Master Thesis

by

Y. Murugesan

to obtain the degree of Master of Science
at the Delft University of Technology,
to be defended publicly on Tuesday August 29th, 2017 at 13:00 PM.

Student number:	4418786	
Project duration:	December 1, 2016 – September 1, 2017	
Thesis committee:	Prof. Dr. ir. L. Nicola,	TU Delft, supervisor
	Prof. Dr. ir. A. Simone,	TU Delft
	Dr. ir. V. Popovich,	TU Delft
	MSc. S.P. Venugopalan,	TU Delft, daily supervisor

Various contact mechanics theories have been developed in recent years. The most popular are the statistical asperity theories of the type of Greenwood and Williamson [1] and Persson's theory [22], which treats self affine rough surfaces. The latter theory includes roughness at all length scales as well as long range elastic interactions. However, it is exact only at full contact conditions, which are often met by rubbers but not by metals. With metals in mind, we here use Green's function molecular dynamics (GFMD) simulations to assess the validity of Persson's theory at small loads, therefore small contact areas. GFMD is a boundary-value method which allows for ultra fine discretization of rough surfaces since it is computationally very efficient, and treats interfacial contact using interatomic potentials. To date, the GFMD method was only used in 3-D for modelling the normal loading of rough elastic semi-infinite incompressible ($\nu = 0.5$) solids [3]. In this work we extend GFMD in order to model both normal and tangential loading of rough solids with finite height and generic elastic properties. GFMD is then used to numerically calculate the proportionality constant κ between the area of real contact a_r and nominal pressure $\bar{p}$ for the contact between a compressible linear elastic solid and a rough rigid punch. The numerically calculated value of the proportionality constant κ is then extrapolated to the thermodynamic, fractal and continuum (TFC) limit. Results are then compared with that of the other analytical models.

Contents

Chapter 1

Introduction

Understanding the contact response of solids with rough surfaces has always been a challenge, it is due to the fact that the solids have self affine rough surfaces with roughness scaling over many decades in length scales. Because of the roughness, when two elastic solids are squeezed together, they do not make contact everywhere in the apparent contact area, but only at a distribution of asperity contact spots. The three physical quantities which characterizes contact mechanics are the contact area fraction a_r, the interfacial separation, and the stress distribution in the contact regions. Determining the area of real contact is a problem of practical importance, as it influences a large number of physical properties namely friction, wear and heat transfer at the interface. It is well known from experiments that there exists a linear relationship between the contact area fraction a_r and the applied nominal pressure $\bar{p}$ for small contact area fractions [4]. Various analytical and numerical models which attempts to predict the relationship between a_r and $\bar{p}$ are discussed below.

The first model of the rough surface contact was too simple for this. It involved the elastic contact between non-interacting uniform spherical asperities with different radii of curvatures on either sides [5]. Using the Hertzian solution for the contact between each asperity, and ignoring friction and adhesion at the interface leads to $a_r \propto \bar{p}^{\frac{2}{3}}$, in disagreement with the experimental linearity.

The first model which incorporated surface statistics was that of Greenwood and willamson (G-W). They represented the rough surface as non interacting uniform spherical asperities having a random distribution of heights [6]. Bush *et al.* extended the G-W theory to include distribution of both heights and radii of curvature (BGT theory) [7].

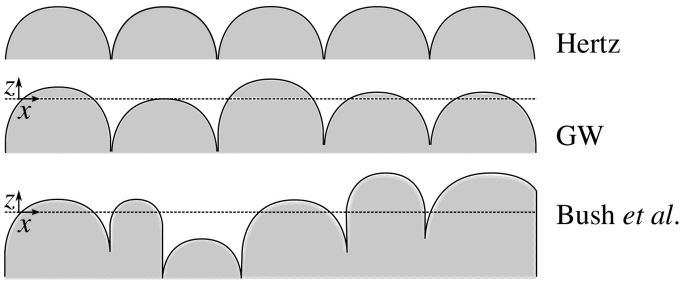

Figure 1.1: Three different models of a rough surface by Hertz [5], Greenwood and Williamson (GW) [1], and Bush *et al.* [7].

The statistical description of the roughness by the above two theories i.e., BGT and G-W lead to the prediction of the linearity between contact area fraction and nominal pressure. However, the lack of the long range elastic interactions lead to the breakdown of the above theories for moderate and high nominal pressures. This lack of long range elastic interactions not only leads to erroneous results but also wrongly predicts that the gap distribution remains Gaussian under loading when it is in-fact exponential.

All the above multiasperity contact theories assumed that the area of real contact has to be much smaller than the nominal contact area. Where as Persson's theory [2] starts from the opposite limit of full contact. Persson derives the analytical expressions for the normal traction probability distribution $P(\sigma, \zeta)$ in the contact area for all the length scales of roughness present at the interface $(\frac{2\pi}{q_L} \leq \frac{2\pi}{q} \leq \frac{2\pi}{q_a})$ where q_L and q_a are the wave-vectors corresponding to the interface width and

atomistic lattice parameter. $P(\sigma, \zeta)$ is expressed as the solution to a diffusion like equation, where the time is replaced by magnification (ζ) and the spatial coordinate by the normal traction σ,

$$\frac{\partial P}{\partial \zeta} = f(\zeta)\frac{\partial^2 P}{\partial \sigma^2} \tag{1.1}$$

The function $f(\zeta)$ carries information about the power spectrum $C(q)$ of the rough surface, the elastic property E and ν of the solids in contact. The physical meaning of the equation for the contact between a rough rigid block and an elastic substrate is as follows: at the lowest magnification ($\zeta = 1$) of the interface, no surface roughness is included at the interface and the block makes an apparent contact with the substrate everywhere in the nominal contact area. Thus the stress distribution for the case is a delta function. Increasing the magnification or adding more and more surface roughness at the interface causes the stress distribution to broaden. Persson's theory predicts a value of $\kappa = \sqrt{\frac{8}{\pi}}$ and is exact for complete contact conditions which are often met by rubbers and not metals. It is also independent of Hurst exponent H, the quantity which is used to characterize the self affinity.

For the contact between elastic semi-infinite solids with non-adhesive interactions, the proportionality constant κ is expressed as,

$$\kappa = \frac{a_r \bar{g} E^*}{\bar{p}} \tag{1.2}$$

where E^* is the effective modulus and $\bar{g}$ is the root mean square gradient and is predicted to be in the range $\sqrt{\frac{\pi}{8}} \leq \kappa \leq \sqrt{2\pi}$.

Over the past decade several numerical contact models of 3-D rough surfaces were developed. The first exhaustive numerical study was performed by Hyun *et al.* [8]. This was a FEM based study on the frictionless contact between elastic solids with self affine rough surfaces. The value of κ is close to Perssons theory for surfaces with $H = 1$. According to Hyun *et al.* [8] the value of κ rises nearly linearly with the Poissons ratio ν and saturates as ν approaches the limiting value of 0.5. The increase in κ with ν is attributed to the increased interactions between nearby asperities. However, the numerical model of Hyun *et al.* [8] has the limitation that it includes only one node per asperity, and according to Yestrabov *et al.* [9], the dependency on the H and overestimation of contact area was due to the poor discretization of the surface (coarser mesh).

More recently a FFT based technique known as the Green's function molecular dynamics (GFMD) was developed which has the advantage of capturing the contact down to the scale of inter-atomic spacing a. Discretizing a surface to such fine scales in FEM simulations will make it computationally expensive. GFMD is a boundary-value method which allows one to simulate the linear-elastic response of a solid to an external load by modeling explicitly only the surface making use of the damped dynamic energy minimization in the Fourier space.

Prodanov *et al.* [3] used the GFMD method to numerically determine κ (κ^{sim}) of rough elastic semi-infinite incompressible ($\nu = 0.5$) solids. As the simulations were performed for a finite size surface with finite discretization the numerically calculated κ^{sim} value was then extrapolated to the

continuum mechanical value κ^{TFC} after introducing the thermodynamic, fractal and continuum corrections. The authors reported a κ^{TFC} value of around 2 and also found a lack of dependency of the Hurst exponent H and thermodynamic corrections.

Previously [3], the GFMD was only used for modelling the normal loading of rough elastic semi-infinite incompressible ($\nu = 0.5$) solids. GFMD was then extended by Venugopalan *et al.* [10] to include shear loading, generic Poisson's ratio and heights. Following this, GFMD was used to rigorously determine the effect of sample heights z_{m}, Poisson's ratio and Hurst exponent on the value of κ^{TFC} [11]. κ^{TFC} was found to be independent of elastic properties and surface topography i.e., E, ν, z_{m} ,$\bar{g}$ and was reported to be around ≈ 1.45. κ^{TFC} for the semi-infinite solid was found to be around half of the previously reported value by Prodanov *et al.* [3]. as the latter did not account for the scaling factor introduced by the DFFT [12].

For modelling the contact of rough surfaces GFMD has a significant computational advantage over FEM or BEM [13], as the latter methods typically require several iterations as well as incremental updating of the boundary conditions in order to converge to the final contact area. GFMD also has the possibility of the usage of more realistic interaction potentials to model the frictional behaviour at the interface. Currently, however the GFMD is limited to modelling the contact response of solids with 1-D rough surfaces (i.e the surface topography is extended into the depth). As the realistic rough surfaces are self affine in 2-D, GFMD must therefore be extended to 3-D in order to model the contact response of solids more realistically.

In this work I adopt the methodology of Venugopalan *et al.* [10] to extend the GFMD. It will be shown in chapter 2 that the GFMD uses the damped dynamics technique to find the equilibrium solution to a mixed boundary value problem and this technique requires the calculation of the elastic restoring force acting on the harmonic modes of the surface layer at each time step. With this in mind, we start with the derivation of the analytical solutions to the displacement fields (in Fourier domain) of a body which is subjected to a displacement prescribed problem. We then calculate the corresponding stress fields inside the body from the well known stress strain relations of linear elastic isotropic solids. The respective analytical solutions are then verified for a sinusoidal displacement prescribed problem.

From the stress and strain fields, the areal elastic energy density of the GFMD layer is analytically derived by calculating the amount of work per unit area needed to deform the elastic slab with surface obeying the small slope approximation. The elastic restoring force in a particular direction is then calculated by taking the derivative of the areal elastic energy density with respect to the displacement in that direction. The correctness of the Green's function matrix which relates the elastic restoring force to the displacement, is then verified by comparing it's limits with the 2-D Green's function matrix derived by Venugopalan *et al.* [10].

Because of the complexity associated in monitoring the equilibration of each and every harmonic mode separately, the equilibration will be collectively verified by validating the GFMD simulation results with that of the FEM for the indentation problem of an elastic slab by a periodic array of flat rigid punches.

Once the GFMD simulation results are validated for the indendation problem, we numerically calculate the κ^{sim} value for the contact between a compressible linear elastic solid ($\nu = 0.33$) and a rough rigid punch with a self-affine roughness of RMS gradient $\bar{g} = 0.01$ and Hurst exponent

$H = 0$. We use a surface with $H = 0$ in order to study the effect of a purely Gaussian surface, which is generated by the power spectral density method in Fourier space. For a Gaussian surface the roughness is characterized by short wavelengths and with the chosen relatively higher value of the continuum discretization ($\epsilon_c = 4$), the surface is not adequately discretized to capture the fine undulations. Hence, the determined κ value is the maximum limit value.

Prodanov *et al.* [3] and Dokkum *et al.* [11] reported a lack of dependency of κ^{TFC} on the thermodynamic correction. Therefore, it was decided to only implement the fractal and continuum corrections to the numerically calculated κ^{sim} value and then extrapolate it to the continuum mechanical limit. We minimize the computational expenses by critically damping the slowest mode. For this we use the critical damping factor derived by Dokkum *et al.* [11].

The remainder of this thesis is organized as follows: In Chapter 2, an in depth introduction to the GFMD method is given. Detailed analytical derivation of the Green's function matrix is shown in Chapter 3. Subsequently, in chapter 4 the GFMD simulation results is validated by comparing them with the FEM. In chapter 5, the proportionality constant κ is determined and compared with the earlier predicted values [6, 7, 2, 14, 15] and numerical simulations [8, 16, 3]. Finally, we give a conclusion of this work in Chapter 6.

Chapter 2

Green's function molecular dynamics

2.1 Introduction

Green's function molecular dynamics (GFMD) is a boundary value method which can be used for simulating the elastic response of a cubic symmetric linear elastic isotropic solid which is subjected to external loading by modelling only the surface. GFMD incorporates the full elastic response of a 3-D solid onto a single surface layer (GFMD layer) so that only the bilinearly coupled surface degrees of freedom interacting via the effective renormalized spring constants have to be considered in the simulations. This greatly increases the computational efficiency as the three dimensional boundary value problem is reduced to a two dimensional problem as shown in the Figure 2.1.

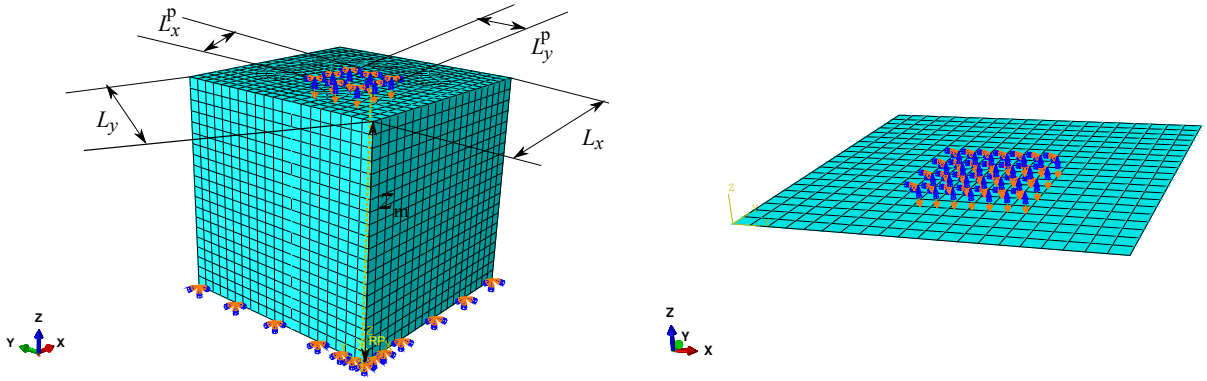

(a) (b)

Figure 2.1: Schematics of the indentation by a flat rigid punch acting on the area $L_x^p L_y^p$ of a) 3-D solid, b) the corresponding GFMD layer .

For a complete traction (displacement) prescribed problem the solution to the displacement (traction) can be obtained by solving the following integral equation

$$u_i(\mathbf{r}) = \int G_{ij}(\mathbf{r} - \mathbf{r}')\sigma_{zj}(\mathbf{r}')d\mathbf{r}', \tag{2.1}$$

where $\mathbf{r}$ is the position vector lying in the surface layer, G_{ij} represents the renormalized effective interactions between the normal and tangential displacements. $\sigma_{zj}(\mathbf{r}')$ is the traction on the surface layer in the j^{th} direction [10]. However, due to the non-local nature of the above integral equation (2.1), using it to solve mixed boundary value problems as the one shown in the Figure (2.1) is computationally expensive. It can be shown that for a $nx \times ny$ discretized surface where nx and ny are the number of discretization points taken at the surface in the x and y directions respectively, it is required to solve $nx \times ny$ equations. The non local nature of the real displacement field can be eliminated by applying Fourier transform to both sides of equation (2.1)

$$\tilde{u}_i(\mathbf{q}) = \sum_j [\tilde{G}(\mathbf{q})]_{ij}\sigma_{zj}(\mathbf{q}), \tag{2.2}$$

where $\tilde{G}_{ij}(\mathbf{q})$ are the Fourier transform of the components of the Green's function matrix. $\tilde{u}_i(\mathbf{q})$

and $\tilde{\sigma}_{zj}(\mathbf{q})$ are the Fourier transforms of $u_i(\mathbf{r})$ and $\sigma_{zi}(\mathbf{r})$ respectively with $\mathbf{q} = \{q_x, q_y\}$

$$\begin{aligned} q_x &= nq_x^{(0)} \quad q_x^{(0)} = \frac{2\pi}{nx}, \\ q_y &= mq_y^{(0)} \quad q_y^{(0)} = \frac{2\pi}{ny}, \end{aligned} \tag{2.3}$$

$q_x^{(0)}$, $q_y^{(0)}$ are the fundamental modes in the x, y directions respectively and n, m are the n^{th}, m^{th} harmonic modes in the x, y directions respectively.

However in the case of a mixed boundary value problem, which is defined as the one where in a part of the surface is traction prescribed and rest is displacement prescribed (Fig. 2.1), the Fourier transformed displacements (tractions) are not known *apriori*. Thus the solution to the displacement is numerically obtained by damped dynamics equilibration.

2.2 Methodology of GFMD

The working methodology of the GFMD technique is explained via the following analogy with the simple harmonic oscillator. A simple spring mass system which is held up by a force f is shown in the Fig. 2.2. Once the force f is released the system oscillates back and forth according to the equation

$$m\frac{d^2u(t)}{dt^2} + ku(t) + \eta v(t) = mg, \tag{2.4}$$

where m corresponds to the mass of the block, k to the spring constant, η to the damping factor of the hydraulic cylinder, $v(t)$ to the velocity of the solid block and g to the acceleration of gravity. The oscillation continues until the energy of the system is minimized, this minimization occurs at the equilibrium position where the weight of the block is balanced by the elastic restoring force $ku(t)$. The rate of convergence to equilibrium is dependent on the damping factor of the system. The equilibrium position of the system can be found by analytically solving the above partial differential equation.

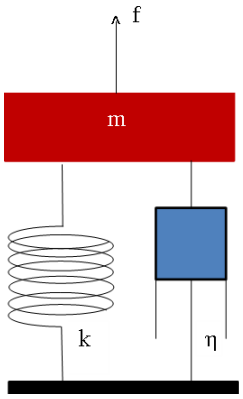

Figure 2.2: Schematic representation of a simple harmonic oscillator.

GFMD models the harmonic modes of the surface layer upon loading to satisfy the following

equation of motion

$$\tilde{\boldsymbol{P}}^{\text{net}}(\mathbf{q}) = m\frac{d^2\tilde{u}(\mathbf{q},t)}{dt^2} = \tilde{\boldsymbol{P}}^{\text{if}}(\mathbf{q},t) + \tilde{\boldsymbol{P}}^{\text{el}}(\mathbf{q},t) + \tilde{\boldsymbol{P}}^{\text{damp}}(\mathbf{q},t), \tag{2.5}$$

where $\tilde{\boldsymbol{P}}^{\text{el}}(\mathbf{q})$ is the elastic restoring force acting in response to the boundary condition imposed on the surface layer. $\tilde{\boldsymbol{P}}^{\text{el}}(\mathbf{q})$ can be calculated using the relation

$$\tilde{\boldsymbol{P}}_i^{\text{el}}(\mathbf{q}) = \frac{dU_{\text{el}}(q)}{du_i(q)} = \sum_j [\tilde{G}^{-1}(\mathbf{q})]_{ij}\tilde{u}_j(\mathbf{q}). \tag{2.6}$$

$\tilde{\boldsymbol{P}}^{\text{if}}(\mathbf{q})$ is the interfacial force which is the implicit force exerted by the punch on the surface of the solid and $\tilde{G}^{-1}(\mathbf{q})$ is the inverse of the Fourier space Green's function matrix. $\tilde{\boldsymbol{P}}^{\text{damp}}(\mathbf{q})$ is the damping force, which enables the system to reach equilibrium. The speed with which a system reaches equilibrium is dependent on whether the system is critically damped or under damped.

Solving a boundary value problem begins with prescribing the boundary conditions onto the discretized surface layer, in the case of a indentation problem this is implicitly done by applying hard-wall interaction condition at the contact of the punch and the surface

$$z_{\text{punch}(x)} \leq z_{\text{(super-)atoms}}(x), \tag{2.7}$$

where $z_{\text{punch}(x)}$ and $z_{\text{(super-)atoms}}$ are the z coordinates of the punch bottom and substrate top respectively. The applied indentation causes the grid points in contact with the punch to be displaced from their initial position to a new configuration. This causes an increase in the areal elastic energy of the system. The numerical minimization of the areal elastic energy is done using the position (Störmer) Verlet (pSV) method [17]. Wherein, the oscillation of the damped harmonic modes is discretized into time steps Δt over the sampling sequence n_{tot} (dimensionless). From displacements $\tilde{u}_n(\mathbf{q})$ and accelerations $\tilde{a}_n(\mathbf{q})$ of a harmonic mode at the n^{th} time step, the displacement $\tilde{u}_{n+1}(\mathbf{q})$ is estimated using the relation

$$\tilde{\boldsymbol{a}}_n(\mathbf{q}) = \frac{\dfrac{\tilde{u}_{n+1}(\mathbf{q}) - \tilde{u}_n(\mathbf{q})}{\Delta t} - \dfrac{\tilde{u}_n(\mathbf{q}) - \tilde{u}_{n-1}(\mathbf{q})}{\Delta t}}{\Delta t}. \tag{2.8}$$

Assuming the mass is set to unity, the above equation can be rewritten as

$$\tilde{u}_{n+1}(\mathbf{q}) = 2\tilde{u}_n(\mathbf{q}) - \tilde{u}_{n-1}(\mathbf{q}) + \tilde{\boldsymbol{a}}_n(\mathbf{q})\Delta t^2. \tag{2.9}$$

The net force acting on each harmonic mode at the $(n+1)^{\text{th}}$ time step is then calculated from equations 2.5 and 2.6. The hard-wall condition is verified at the end of each iteration step and whenever it is violated, the (super-)atoms are moved back to the punch surface. The above steps are looped until equilibrium is reached. Once equilibrium is reached, the damping force goes to zero because the displacements $\tilde{u}_{n+1}(\mathbf{q})$ and $\tilde{u}_n(\mathbf{q})$ are equal. It is necessary to make the system critically damped or under-damped in order to converge to the correct solution.

It will be shown in Sec. 5.2 that the determination of proportionality constant κ between the area fraction and load requires a wide range of simulations involving the indentation of a flat surface by a rough rigid indenter. A 2048×2048 discretized GFMD layer with the $\tilde{u}_x(0,0)$ mode critically damped takes nearly 5 hrs to equilibrate. To minimize the computation time we use the appropriate critical damping factor for each mode. Recently a mode dependent critical vector

damping factor $\tilde{\eta}_{\mathrm{cr},i}(\mathbf{q})$ was derived analytically by Dokkum *et al.* [11]. The authors start with writing the explicit velocity and position forms of the pSV equations

$$\tilde{\boldsymbol{v}}_{n+1}(\mathbf{q}) = \tilde{\boldsymbol{P}}_n^{\mathrm{el}}(\Delta t) - \tilde{\boldsymbol{v}}_n(1 - \eta(\Delta t^2)) \tag{2.10}$$

$$\tilde{\boldsymbol{u}}_{n+1}(\mathbf{q}) = \tilde{\boldsymbol{u}}_n(\mathbf{q}) + \tilde{\boldsymbol{P}}_n^{\mathrm{el}}(\Delta t)^2 - \tilde{\boldsymbol{v}}_n(\Delta t - \eta(\Delta t^3)) \tag{2.11}$$

as a matrix difference equation in general form

$$\begin{bmatrix} \tilde{\boldsymbol{u}}_{n+1}(\mathbf{q}) \\ \tilde{\boldsymbol{v}}_{n+1}(\mathbf{q}) \end{bmatrix} = \begin{bmatrix} \vartheta \end{bmatrix} \begin{bmatrix} \tilde{\boldsymbol{u}}_n(\mathbf{q}) \\ \tilde{\boldsymbol{v}}_n(\mathbf{q}) \end{bmatrix}. \tag{2.12}$$

The different dynamic characteristic regimes of the damped harmonic oscillator in the velocity Verlet method are determined through the eigen values of the matrix ϑ. The authors showed that for a critically damped system, the eigen values of the matrix must be equal and also found the damping factor to be a function of elastic modulus E, poisson's ratio ν, dimensions of the unit cell and discrete time step Δt. It was analytically proven by them that the slowest mode is the first mode. Therefore they used the damping factor $\tilde{\eta}_{\mathrm{cr},i}(\mathbf{q})$ of the first mode to damp all other modes

$$\eta_{1,\mathrm{cr}}(\mathbf{q} = 0, z_{\mathrm{m}}) = 2\frac{\sqrt{\kappa_1}}{\Delta t} - \kappa_1, \tag{2.13}$$

where,

$$\kappa_1(\mathbf{q} = 0, z_{\mathrm{m}}) = \frac{C_{44}}{z_{\mathrm{m}}}. \tag{2.14}$$

Using the above scalar damping factor resulted in the first mode being critically damped and all other modes being under damped.

Note, the GFMD technique is not only limited to hard-wall interaction but also offers the possibility of including a broader range of potentials. Herein, we briefly discuss about various potentials which are so far only used to model the delamination phenomena as one of the many possible candidates to describe the friction behaviour. The most commonly implemented mixed mode cohesive zone interaction potential was developed by Xu and Needleman [18]. This potential is physically realistic only for the case where in the ratio of tangential to normal work of indentation (separation) $(\frac{\phi_t}{\phi_n})$ is set to unity, however the above assumption is in total disagreement with the experimental results [19]. The BSG model which is a non-potential based extension of the above model with $(\phi_t \neq \phi_n)$ is physically realistic for mixed mode separation problems [20]. However the model predicts physically unrealistic mixed mode coupling behaviour for indentation problems i.e it predicts repulsive tangential tractions for significant over-closure, thus making it unsuitable for the prediction of proportionality constant κ. The latest non-potential model developed by Mcgarry *et al.* [21] correctly predicts the mixed mode coupling between tangential and normal tractions for both indentation and separation problems. Note, that the current work is restricted to the usage of hard-wall boundary condition mainly because of the inherent simplicity associated with estimating the contact area fraction.

2.3 Pseudo code

1. Setup rigid punch with surface topography $h(x)$.
2. Determine damping factor vector η_{cr} such that all modes are critically and/or under-damped,

and calculate the dimensionless equilibrium time t_{equil}.
3. Give the rigid punch initial displacement in normal direction, i.e., $z_{\text{punch}} = h(x) - \delta_x$, where δ_x is the finite indentation depth.
4. Loop over dimensionless time-step Δt till the equilibrium time t_{equil} is reached.

- Discretize the surface layer in the real space with $nx \times ny$ nodes.
- Discrete fast Fourier transform (DFFT) the surface displacement $u_i(\mathbf{r})$ using the FFTW3 library, $\mathscr{F}(u_i(\mathbf{r})) = \tilde{u}_i(\mathbf{q})$, where $\mathbf{r}$ is the position vector of the surface nodes.
- Calculate the elastic restoring force $\boldsymbol{P}^{\text{el}}(\mathbf{q})$ (refer equation 2.6).
- Calculate the damping force term $\tilde{\boldsymbol{P}}^{\text{damp}}(\mathbf{q})$ and add it to the elastic restoring force,

$$\tilde{\boldsymbol{P}}^{\text{damp}}(\mathbf{q}) = \eta(\tilde{u}_n(\mathbf{q}) - \tilde{u}_{n-1}(\mathbf{q})), \tag{2.15}$$

$$\tilde{\boldsymbol{P}}(\mathbf{q}) = \tilde{\boldsymbol{P}}^{\text{el}}(\mathbf{q}) + \tilde{\boldsymbol{P}}^{\text{damp}}(\mathbf{q}) \tag{2.16}$$

- Use pSV to numerically solve the equation of motion (equation 2.5),

$$\tilde{u}_{n+1}(\mathbf{q}) = 2\tilde{u}_n(\mathbf{q}) - \tilde{u}_{n-1}(\mathbf{q}) + \tilde{\boldsymbol{P}}(\mathbf{q})\Delta t^2 \tag{2.17}$$

- Converted the displacements back to the real space and implemented the boundary condition through the hard-wall rule given by

$$u_{n+1}(\mathbf{r}) \leftarrow \max\{u_{n+1}(\mathbf{r}), z_{\text{punch}}\}, \tag{2.18}$$

- Iterate the above steps until equilibrium is reached.

Chapter 3

Analytical derivation of the 3-D Green's function matrix for finite height linear elastic solid

3.1 Introduction

The elastic energy density of the GFMD layer is analytically derived by calculating the amount of work per unit area needed to deform the elastic slab with small-slope at the surface. The elastic restoring force in a particular direction is then calculated by taking the derivative of the areal elastic energy density with respect to the displacement in that direction

$$P_i^{\mathrm{el}}(q) = \frac{dU_{\mathrm{el}}(q)}{du_i(q)} = \sum_j [\tilde{G}^{-1}(\mathbf{q})]_{ij} \tilde{u}_j(\mathbf{q}). \tag{3.1}$$

The work presented in this chapter is organized as follows: we report the methodology used by Venugopalan *et al.* [10] to find the analytical solution of the areal elastic energy of a 2-D elastic slab. We start with the derivation of the analytical solutions to the displacement fields (in Fourier domain) in 3-D. We then calculate the corresponding stress fields from the well known stress strain relations of a linear isotropic solid and the respective analytical solutions are then verified for a sinusoidal displacement prescribed problem. The areal elastic energy density and thereby the Green's function matrix which relates the elastic restoring force to the displacement is derived and the components of the 3-D Green's function matrix are verified by comparing it's limits with that of the 2-D Green's function matrix derived by Venugopalan *et al.* [10].

3.2 2-D areal elastic energy density

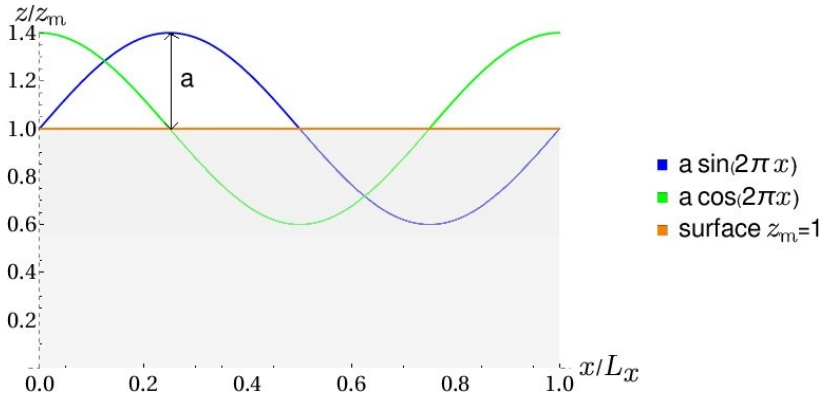

Figure 3.1: Deformation by a single mode displacement.

Here, we firstly report the derivation of the areal elastic energy density of an elastic slab with generic elastic properties following the methodology of Venugopalan *et al.* [10]. Assuming that a single mode loading is prescribed in the z direction at the surface of a slab (Fig. 3.1) with fixed bottom $u_i(x, z = 0) = 0$. The analytical solution to the displacements $u_x(x, z)$ and $u_z(x, z)$ is obtained through solving the equilibrium equation of forces

$$\begin{aligned} \left[C_{44}\left(\partial_3^2\right) + C_{11}\partial_1^2\right] u_x(x,z) + \left(C_{12} + C_{44}\right)\partial_3\partial_1 u_z(x,z) = 0, \\ \left[C_{44}C_{11}\partial_3^2\right] u_z(x,z) + \left(C_{12} + C_{44}\right)\partial_3\partial_1 u_x(x,z) = 0, \end{aligned} \tag{3.2}$$

in the Fourier space

$$\begin{aligned} &s\left[(iq_x)\frac{\partial\tilde{u}_z(q_x,z)}{\partial z}+\frac{\partial^2\tilde{u}_x(q_x,z)}{\partial z^2}\right] \quad +(1-2s)\left[(iq_x)\frac{\partial\tilde{u}_z(q_x,z)}{\partial z}\right]+(iq_x)^2\tilde{u}_x(q_x,z), \\ &s\left[(iq_x)^2\tilde{u}_z(q_x,z)+(iq_x)\frac{\partial\tilde{u}_x(q_x,z)}{\partial z}\right]+\frac{\partial^2\tilde{u}_z(q_x,z)}{\partial z^2}+ \quad (1-2s)\left[(iq_x)\frac{\partial\tilde{u}_x(q_x,z)}{\partial z}\right]. \end{aligned} \tag{3.3}$$

Here, $\tilde{u}_x(q_x,z)$, $\tilde{u}_y(q_x,z)$, $\tilde{u}_z(q_x,z)$ are the amplitudes of the Fourier transforms of $u_x(x,\ z)$, $u_y(x,\ z)$, $u_z(x,\ z)$ respectively at the position (q_x) in the Fourier domain. $s=\dfrac{C_{44}}{C_{11}}$ and C_{ij} are the coefficients of the elastic tensor.
Solution to the above ordinary differential equations is as follows,

$$\begin{bmatrix} \tilde{u}_x(\mathbf{q},z) \\ \tilde{u}_z(\mathbf{q},z) \end{bmatrix} = \begin{bmatrix} f_1(q_x,q_y,z) & -if_3(q_x,q_y,z) \\ if_3(q_x,q_y,z) & f_6(q_x,q_y,z) \end{bmatrix} \begin{bmatrix} a_1 \\ a_2 \end{bmatrix}, \tag{3.4}$$

Detailed expressions of the matrix components f_i can be found in the work of Venugopalan *et al.* [10]. Once the solution to the displacement is known, the areal elastic energy density $U_{\mathrm{el}}(q)$ is found by calculating the amount of work per unit area needed to deform the surface

$$\begin{aligned} U_{\mathrm{el}}(q) = &\frac{1}{L}\int_0^L \sigma_{zx}(x,z_{\mathrm{m}})\{\tilde{u}_x(q,z_{\mathrm{m}})e^{\mathrm{i}qx}+\tilde{u}_x(-q,z_{\mathrm{m}})e^{-\mathrm{i}qx}\}dx \\ &+\frac{1}{L}\int_0^L \sigma_{zz}(x,z_{\mathrm{m}})\{\tilde{u}_z(q,z_{\mathrm{m}})e^{\mathrm{i}qx}+\tilde{u}_z(-q,z_{\mathrm{m}})e^{-\mathrm{i}qx}\}dx. \end{aligned} \tag{3.5}$$

Substituting for the stresses $\sigma_{zx}(x,z_{\mathrm{m}})$, $\sigma_{zz}(x,z_{\mathrm{m}})$ and integrating the above equation within the limits [0,1], the expression for the areal elastic energy density reads

$$U_{\mathrm{el}}(q) = \begin{bmatrix} \tilde{u}_x(-q,z_{\mathrm{m}}) & \tilde{u}_z(-q,z_{\mathrm{m}}) \end{bmatrix} \begin{bmatrix} M_{xx}(q,z_{\mathrm{m}}) & \mathrm{i}M_{xz}(q,z_{\mathrm{m}}) \\ -\mathrm{i}M_{xz}(q,z_{\mathrm{m}}) & M_{zz}(q,z_{\mathrm{m}}) \end{bmatrix} \begin{bmatrix} \tilde{u}_x(q,z_{\mathrm{m}}) \\ \tilde{u}_z(q,z_{\mathrm{m}}) \end{bmatrix} \tag{3.6}$$

here

$$\begin{aligned} M_{xx} &= \frac{C_{11}q[1-r]\left[\sinh(qz_{\mathrm{m}})\cosh(qz_{\mathrm{m}})-rqz_{\mathrm{m}}\right]}{2\left[-r^2qz_{\mathrm{m}}^2+\cosh^2(qz_{\mathrm{m}})-1\right]}, \\ M_{xz} &= \frac{C_{11}q[1-r]\left[(1-r)\sinh^2(qz_{\mathrm{m}})-2r^2qz_{\mathrm{m}}^2\right]}{2[r+1]\left[-r^2qz_{\mathrm{m}}^2+\cosh^2(qz_{\mathrm{m}})-1\right]}, \\ M_{zz} &= \frac{C_{11}q[1-r]\left[rqz_{\mathrm{m}}+\sinh(qz_{\mathrm{m}})\cosh(qz_{\mathrm{m}})\right]}{2\left[-r^2qz_{\mathrm{m}}^2+\cosh^2(qz_{\mathrm{m}})-1\right]}. \end{aligned} \tag{3.7}$$

Applying the concept of Fourier transform, any arbitrary displacement $u_z(x,z_{\mathrm{m}})$ could be broken down into a wide range of single modes with varying frequencies

$$\begin{aligned} u_z(x,z_{\mathrm{m}}) &= \sum_q \tilde{u}_z(q,z_{\mathrm{m}})e^{\mathrm{i}qx}+\tilde{u}_z(-q,z_{\mathrm{m}})e^{-\mathrm{i}qx}, \\ \tilde{u}_z(q,z_{\mathrm{m}}) = \frac{\tilde{u}_z^{\mathrm{c}^0}(q,z_{\mathrm{m}})-\mathrm{i}\tilde{u}_z^{\mathrm{s}^0}(q,z_{\mathrm{m}})}{2}, &\quad \tilde{u}_z(-q,z_{\mathrm{m}}) = \frac{\tilde{u}_z^{\mathrm{c}^0}(q,z_{\mathrm{m}})+\mathrm{i}\tilde{u}_z^{\mathrm{s}^0}(q,z_{\mathrm{m}})}{2} \end{aligned} \tag{3.8}$$

here, $\tilde{u}_z^{\mathrm{c}^0}(q,z_{\mathrm{m}})$ is the maximum amplitude of the cosine part of the prescribed displacement, $\tilde{u}_z^{\mathrm{s}^0}(q,z_{\mathrm{m}})$ is the maximum amplitude of the sine part of the prescribed displacement. Using the

above relation for $\tilde{u}_z(q, z_\mathrm{m})$ and $\tilde{u}_z(-q, z_\mathrm{m})$ i.e the amplitudes of the Fourier transform of $u_z(x, z_\mathrm{m})$ at frequencies q and $-q$ respectively, the prescribed displacement $u_z(x, z_\mathrm{m})$ reduces to the following form

$$u_z(x, z_\mathrm{m}) = \sum_q \tilde{u}_z^{\mathrm{c}^0}(q, z_\mathrm{m})\cos(qx) + \tilde{u}_z^{\mathrm{s}^0}(q, z_\mathrm{m})\sin(qx). \tag{3.9}$$

Similar to the case of the displacement, the areal elastic energy density (equation 3.6) can then be expressed as a summation over different modes.

3.3 3-D analytical solution of the displacement

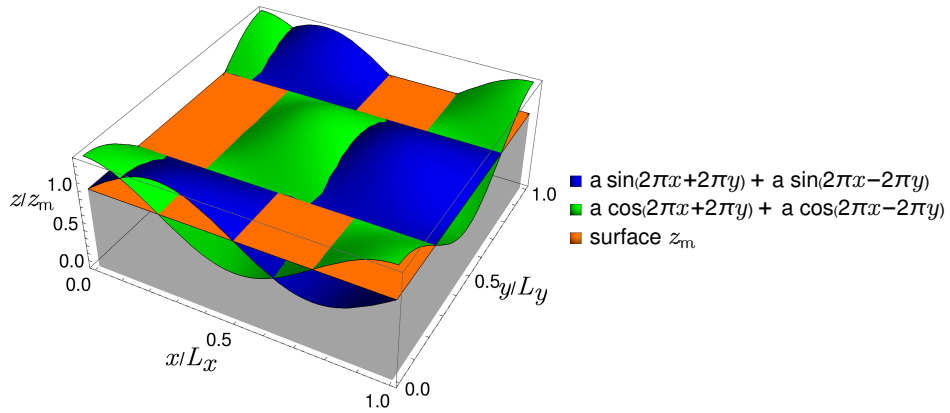

Figure 3.2: Deformation by a single mode displacement.

Following the methodology mentioned in the previous section 3.2, the analytical solution to the displacements $u_x(x, y, z)$, $u_y(x, y, z)$ and $u_z(x, y, z)$ when a single modal 2-D displacement is prescribed at the surface (Fig. 3.2) can be obtained by solving the equilibrium equation

$$\begin{aligned}
\left[C_{44}\left(\partial_3^2 + \partial_2^2\right) + C_{11}\partial_1^2\right] u_x(x, y, z) + (C_{12} + C_{44})\,\partial_1\partial_2\; u_y(x, y, z) + (C_{12} + C_{44})\,\partial_3\partial_1 u_z(x, y, z) = 0,\\
\left[C_{44}\left(\partial_1^2 + \partial_3^2\right) + C_{11}\partial_2^2\right] u_y(x, y, z) + (C_{12} + C_{44})\,\partial_1\partial_2 u_x(x, y, z) + (C_{12} + C_{44})\,\partial_3\partial_2 u_z(x, y, z) = 0,\\
\left[C_{44}\left(\partial_1^2 + \partial_2^2\right) + C_{11}\partial_3^2\right] u_z(x, y, z) + (C_{12} + C_{44})\,\partial_3\partial_2 u_y(x, y, z) + (C_{12} + C_{44})\,\partial_3\partial_1 u_x(x, y, z) = 0,
\end{aligned} \tag{3.10}$$

in Fourier domain,

$$
\begin{aligned}
&s\left[(iq_y)^2\tilde{u}_x(\mathbf{q},z)+(iq_x)(iq_y)\tilde{u}_y(\mathbf{q},z)+(iq_x)\frac{\partial\tilde{u}_z(\mathbf{q},z)}{\partial z}+\frac{\partial^2\tilde{u}_x(\mathbf{q},z)}{\partial z^2}\right]\\
&\quad+(1-2s)\left[(iq_x)(iq_y)\tilde{u}_y(\mathbf{q},z)+(iq_x)\frac{\partial\tilde{u}_z(\mathbf{q},z)}{\partial z}\right]+(iq_x)^2\tilde{u}_x(\mathbf{q},z),\\
&s\left[(iq_x)^2\tilde{u}_y(\mathbf{q},z)+(iq_y)(iq_x)\tilde{u}_x(\mathbf{q},z)+(iq_y)\frac{\partial\tilde{u}_z(\mathbf{q},z)}{\partial z}+\frac{\partial^2\tilde{u}_y(\mathbf{q},z)}{\partial z^2}\right]\\
&\quad+(1-2s)\left[(iq_x)(iq_y)\tilde{u}_x(\mathbf{q},z)+(iq_y)\frac{\partial\tilde{u}_z(\mathbf{q},z)}{\partial z}\right]+(iq_y)^2\tilde{u}_y(\mathbf{q},z),\\
&s\left[(iq_x)^2\tilde{u}_z(\mathbf{q},z)+(iq_y)^2\tilde{u}_z(\mathbf{q},z)+(iq_x)\frac{\partial\tilde{u}_x(\mathbf{q},z)}{\partial z}+(iq_y)\frac{\partial\tilde{u}_y(\mathbf{q},z)}{\partial z}\right]+\frac{\partial^2\tilde{u}_z(\mathbf{q},z)}{\partial z^2}\\
&\quad+\quad(1-2s)\left[(iq_x)\frac{\partial\tilde{u}_x(\mathbf{q},z)}{\partial z}+(iq_y)\frac{\partial\tilde{u}_y(\mathbf{q},z)}{\partial z}\right],
\end{aligned}
\tag{3.11}
$$

here $\tilde{u}_x(\mathbf{q},z)$, $\tilde{u}_y(\mathbf{q},z)$, $\tilde{u}_z(\mathbf{q},z)$ are the amplitudes of the Fourier transforms of $u_x(x,\ y,\ z)$, $u_y(x,\ y,\ z)$, $u_z(x,\ y,\ z)$ respectively at the position $(q_x,\ q_y)$ in the Fourier domain. Solution to the above ordinary differential equations with the constraint $u_i(x,\ y,\ 0)=0$ is as follows,

$$
\begin{bmatrix}\tilde{u}_x(\mathbf{q},z)\\ \tilde{u}_y(\mathbf{q},z)\\ \tilde{u}_z(\mathbf{q},z)\end{bmatrix}=\begin{bmatrix}f_1(q_x,q_y,z) & f_2(q_x,q_y,z) & f_3(q_x,q_y,z)\\ f_2(q_x,q_y,z) & f_4(q_x,q_y,z) & f_5(q_x,q_y,z)\\ f_3(q_x,q_y,z) & f_5(q_x,q_y,z) & f_6(q_x,q_y,z)\end{bmatrix}\begin{bmatrix}a_1\\ a_2\\ a_3\end{bmatrix},
$$

here

$$
\begin{aligned}
f_1(q_x,q_y,z)&=\frac{q_x^2\left[(s+1)\sinh(q_{\mathrm{r}}z)-q_{\mathrm{r}}(s-1)z\cosh(q_{\mathrm{r}}z)\right]+q_y^2\cosh(q_{\mathrm{r}}z)}{2\left(q_x^2+q_y^2\right)^{3/2}},\\
f_2(q_x,q_y,z)&=\frac{q_xq_y[s-1]\left[\sinh(q_{\mathrm{r}}z)-q_{\mathrm{r}}z\cosh(q_{\mathrm{r}}z)\right]}{2\left(q_x^2+q_y^2\right)^{3/2}},\\
f_3(q_x,q_y,z)&=\frac{[iq_x(s-1)z\sinh(q_{\mathrm{r}}z)]}{2q_{\mathrm{r}}},\\
f_4(q_x,q_y,z)&=\frac{q_y^2\left[(s+1)\sinh(q_{\mathrm{r}}z)-q_{\mathrm{r}}(s-1)z\cosh(q_{\mathrm{r}}z)\right]+2q_x^2\sinh(q_{\mathrm{r}}z)}{2\left(q_x^2+q_y^2\right)^{3/2}},\\
f_5(q_x,q_y,z)&=\frac{[iq_y(s-1)z\sinh(q_{\mathrm{r}}z)]}{2q_{\mathrm{r}}},\\
f_6(q_x,q_y,z)&=\frac{[(s+1)\sinh(q_{\mathrm{r}}z)+q_{\mathrm{r}}(s-1)z\cosh(q_{\mathrm{r}}z)]}{2q_{\mathrm{r}}}.
\end{aligned}
\tag{3.12}
$$

Here $q_{\mathrm{r}}=\sqrt{q_x^2+q_y^2}$, the terms a_1, a_2 and a_3 can be obtained by substituting in equation 4.10 the Fourier space amplitudes of the prescribed boundary condition $u_i(x,y,z)$.
A single modal 2-D displacement $u_z(x,y,z_{\mathrm{m}})$ that is prescribed at the surface is given as,

$$
\begin{aligned}
u_z(x,y,z_{\mathrm{m}})=&\,\tilde{u}_z\left(q_x,q_y,z_{\mathrm{m}}\right)e^{\mathrm{i}(q_xx+q_yy)}+\tilde{u}_z\left(-q_x,-q_y,z_{\mathrm{m}}\right)e^{-\mathrm{i}(q_xx+q_yy)}\\
&+\tilde{u}_z\left(q_x,-q_y,z_{\mathrm{m}}\right)e^{\mathrm{i}(q_xx-q_yy)}+\tilde{u}_z\left(-q_x,q_y,z_{\mathrm{m}}\right)e^{-\mathrm{i}(q_xx-q_yy)}.
\end{aligned}
\tag{3.13}
$$

substituting the above boundary condition in equation 4.10, the Fourier space displacements at any arbitrary height can be calculated. Once the displacements are known the stresses and strains can be calculated using the stress strain relationships of a linear elastic solid

$$\begin{bmatrix} \tilde{\sigma}_x(\mathbf{q},z) \\ \tilde{\sigma}_y(\mathbf{q},z) \\ \tilde{\sigma}_z(\mathbf{q},z) \\ \tilde{\sigma}_{xy}(\mathbf{q},z) \\ \tilde{\sigma}_{yz}(\mathbf{q},z) \\ \tilde{\sigma}_{zx}(\mathbf{q},z) \end{bmatrix} = \begin{bmatrix} C_{11} & C_{12} & C_{12} & 0 & 0 & 0 \\ C_{12} & C_{11} & C_{12} & 0 & 0 & 0 \\ C_{12} & C_{12} & C_{11} & 0 & 0 & 0 \\ 0 & 0 & 0 & C_{44} & 0 & 0 \\ 0 & 0 & 0 & 0 & C_{44} & 0 \\ 0 & 0 & 0 & 0 & 0 & C_{44} \end{bmatrix} \begin{bmatrix} \tilde{\epsilon}_{xx}(\mathbf{q},z) \\ \tilde{\epsilon}_{yy}(\mathbf{q},z) \\ \tilde{\epsilon}_{zz}(\mathbf{q},z) \\ \tilde{\epsilon}_{xy} \\ \tilde{\epsilon}_{yz} \\ \tilde{\epsilon}_{zx} \end{bmatrix},$$

$$\begin{bmatrix} \tilde{\epsilon}_{xx}(\mathbf{q},z) \\ \tilde{\epsilon}_{yy}(\mathbf{q},z) \\ \tilde{\epsilon}_{zz}(\mathbf{q},z) \\ \tilde{\epsilon}_{xy} \\ \tilde{\epsilon}_{yz} \\ \tilde{\epsilon}_{zx} \end{bmatrix} = \begin{bmatrix} (iq_x)\tilde{u}_x(\mathbf{q},z) \\ (iq_y)\tilde{u}_y(\mathbf{q},z) \\ \dfrac{\partial u_z(\mathbf{q},z)}{\partial z} \\ (iq_y)\tilde{u}_x(\mathbf{q},z) + (iq_x)\tilde{u}_y(\mathbf{q},z) \\ \dfrac{\partial u_x(\mathbf{q},z)}{\partial z} + (iq_x)\tilde{u}_z(\mathbf{q},z) \\ \dfrac{\partial u_y(\mathbf{q},z)}{\partial z} + (iq_y)\tilde{u}_z(\mathbf{q},z) \end{bmatrix} \tag{3.14}$$

The analytical solutions of stress, strain and displacement are verified by comparing the body fields for a displacement prescribed problem with known solution. When a sinusoidal displacement is prescribed in the normal direction at the surface of a 3-D solid with restricted tangential displacements i.e ($u_z(x,y,z_\mathrm{m}) = u_0$ and $u_x(x,y,z_\mathrm{m}) = 0$, $u_y(x,y,z_\mathrm{m}) = 0$), it is well known that the in-plane cosine transform of the tangential displacements $u_x(x,y,z)$ and $u_y(x,y,z)$ couples with the in-plane sine transform of the normal displacement $u_z(x,y,z)$. Figures 3.3, 3.4 and 3.5 show the analytical solution of the displacement fields. Figures 3.6, 3.8 and 3.7 show the analytical solution of the corresponding strain fields. The inherent periodicity of the problem is well evident with the body fields repeating in both the x and y directions. Additionally the symmetry of the problem is also well evident in these body fields, one example is the rotational symmetry of the lateral displacement fields $u_x(x,y,z)$ and $u_y(x,y,z)$.

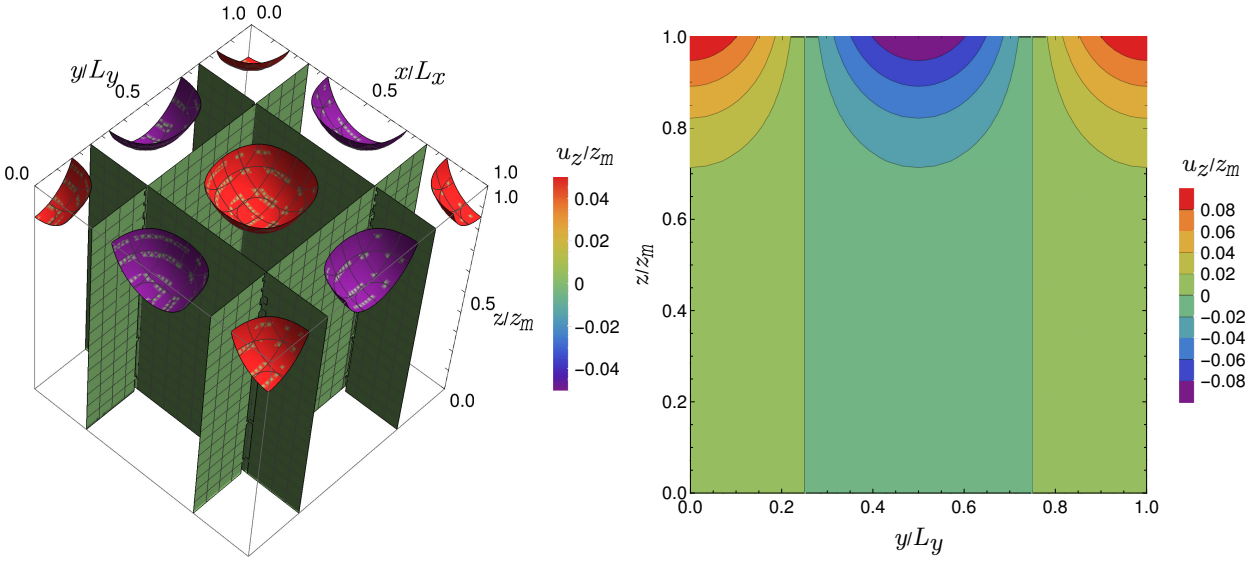

(a) (b)

Figure 3.3: Analytical solution of displacement fields a) $\frac{u_z}{z_\mathrm{m}}(\frac{x}{L_x}, \frac{y}{L_y}, \frac{z}{z_\mathrm{m}})$, b) $\frac{u_z}{z_\mathrm{m}}(\frac{x}{L_x} = 0, \frac{y}{L_y}, \frac{z}{z_\mathrm{m}})$.

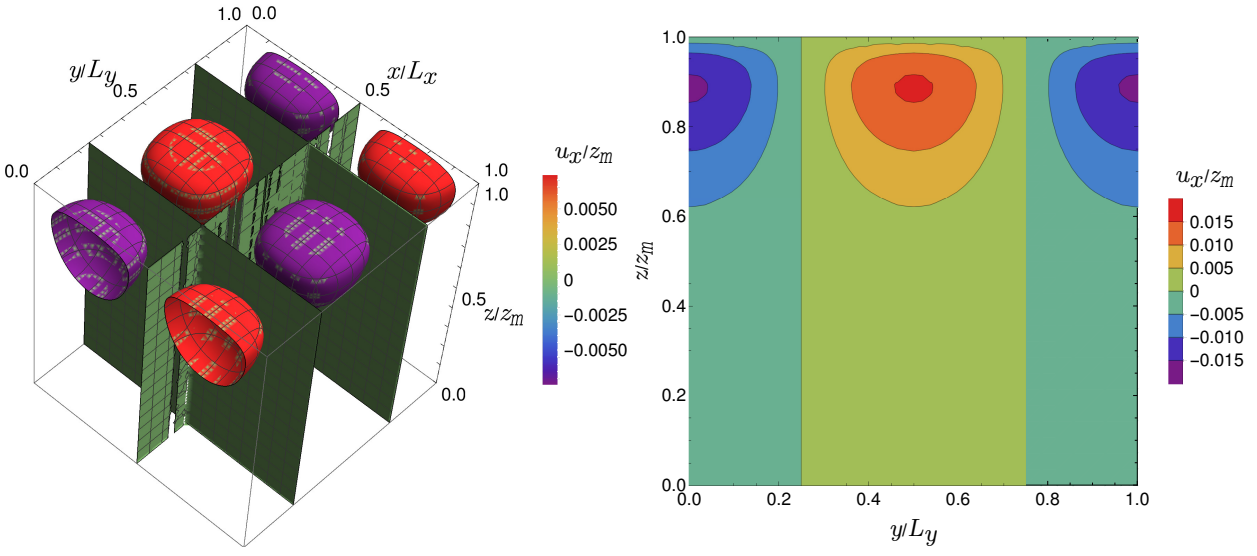

(a) (b)

Figure 3.4: Analytical solution of displacement fields a) $\frac{u_x}{z_\mathrm{m}}(\frac{x}{L_x}, \frac{y}{L_y}, \frac{z}{z_\mathrm{m}})$, b) $\frac{u_x}{z_\mathrm{m}}(\frac{x}{L_x} = 0.25, \frac{y}{L_y}, \frac{z}{z_\mathrm{m}})$.

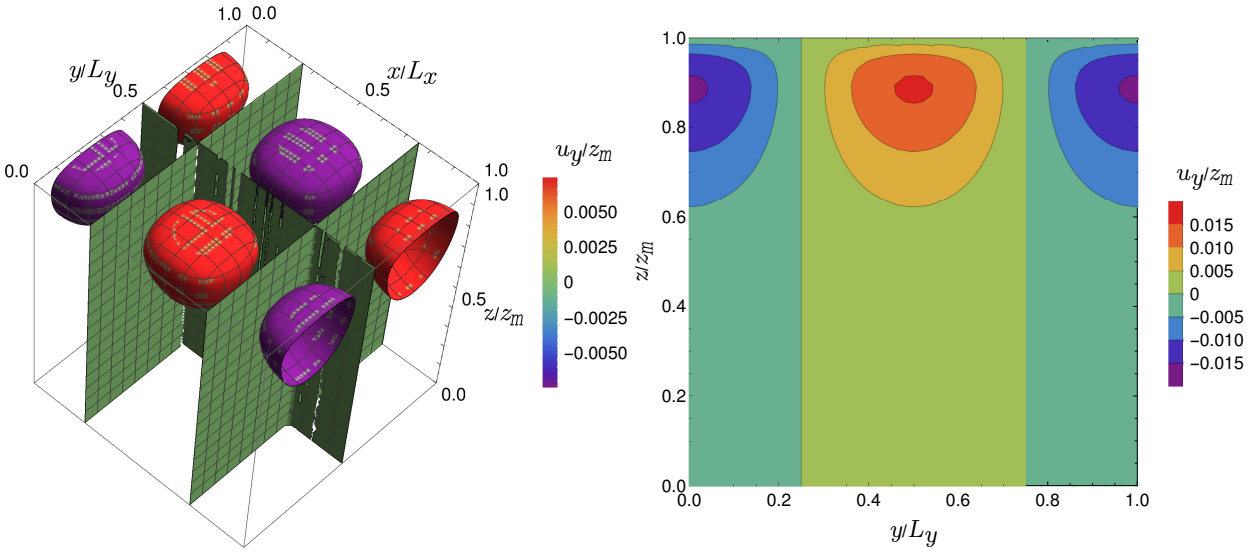

(a) (b)

Figure 3.5: Analytical solution of displacement fields a) $\frac{u_y}{z_\mathrm{m}}(\frac{x}{L_x}, \frac{y}{L_y}, \frac{z}{z_\mathrm{m}})$, b) $\frac{u_y}{z_\mathrm{m}}(\frac{x}{L_x}, \frac{y}{L_y} = 0.25, \frac{z}{z_\mathrm{m}})$.

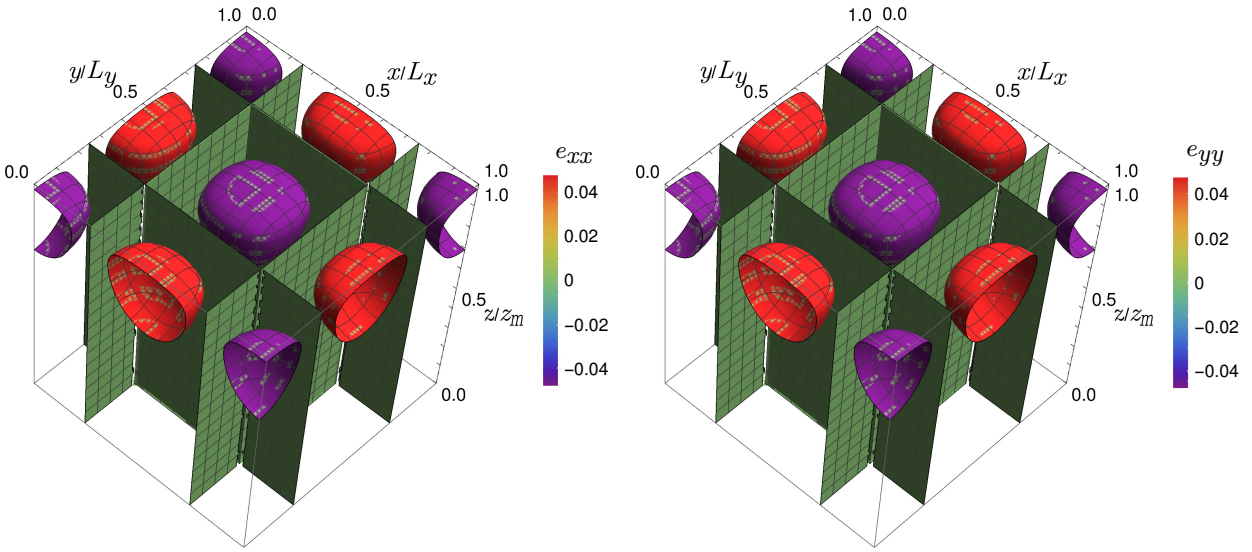

(a) (b)

Figure 3.6: Analytical solution of strain fields a) $e_{xx}(\frac{x}{L_x}, \frac{y}{L_y}, \frac{z}{z_\mathrm{m}})$, b) $e_{yy}(\frac{x}{L_x}, \frac{y}{L_y}, \frac{z}{z_\mathrm{m}})$.

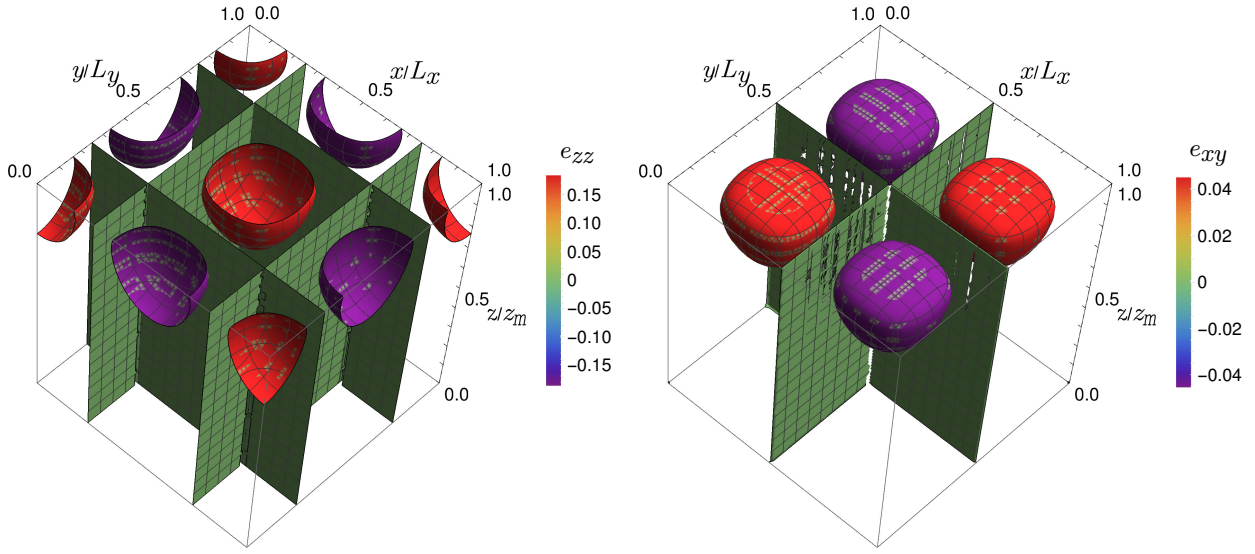

(a) (b)

Figure 3.7: Analytical solution of strain fields a) $e_{zz}(\frac{x}{L_x}, \frac{y}{L_y}, \frac{z}{z_{\mathrm{m}}})$, b) $e_{xy}(\frac{x}{L_x}, \frac{y}{L_y}, \frac{z}{z_{\mathrm{m}}})$.

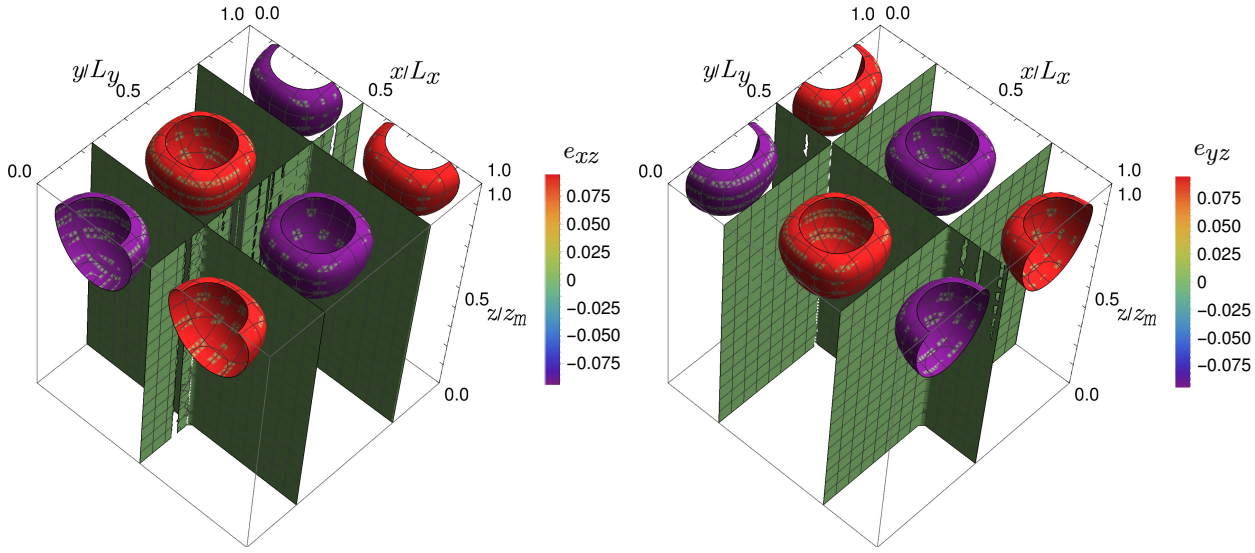

(a) (b)

Figure 3.8: Analytical solution of strain fields a) $e_{xz}(\frac{x}{L_x}, \frac{y}{L_y}, \frac{z}{z_{\mathrm{m}}})$, b) $e_{yz}(\frac{x}{L_x}, \frac{y}{L_y}, \frac{z}{z_{\mathrm{m}}})$.

3.4 3-D areal elastic energy density

The areal elastic energy density U_{el} is obtained by finding the amount of work per unit area needed to deform the elastic slab assuming that the indenter satisfies the small slope approximation

$$
\begin{aligned}
U_{\mathrm{el}}(\mathbf{q}) = & \frac{2C_{44}}{2L_xL_y}\int_0^{L_y}\int_0^{L_x}\tilde{\epsilon}_{xz}\left(x,y,z_{\mathrm{m}}\right)\left[\sum_{q_x,-q_x}\sum_{q_y,-q_y}\tilde{u}_x\left(q_x,q_y,z_{\mathrm{m}}\right)e^{\mathrm{i}(q_xx+q_yy)}\right]dxdy \\
& +\frac{2C_{44}}{2L_xL_y}\int_0^{L_y}\int_0^{L_x}\tilde{\epsilon}_{yz}\left(x,y,z_{\mathrm{m}}\right)\left[\sum_{q_x,-q_x}\sum_{q_y,-q_y}\tilde{u}_y\left(q_x,q_y,z_{\mathrm{m}}\right)e^{\mathrm{i}(q_xx+q_yy)}\right]dxdy \\
& +\frac{C_{12}}{2L_xL_y}\int_0^{L_y}\int_0^{L_x}\tilde{\epsilon}_{xx}\left(x,y,z_{\mathrm{m}}\right)\left[\sum_{q_x,-q_x}\sum_{q_y,-q_y}\tilde{u}_z\left(q_x,q_y,z_{\mathrm{m}}\right)e^{\mathrm{i}(q_xx+q_yy)}\right]dxdy \\
& +\frac{C_{12}}{2L_xL_y}\int_0^{L_y}\int_0^{L_x}\tilde{\epsilon}_{yy}\left(x,y,z_{\mathrm{m}}\right)\left[\sum_{q_x,-q_x}\sum_{q_y,-q_y}\tilde{u}_z\left(q_x,q_y,z_{\mathrm{m}}\right)e^{\mathrm{i}(q_xx+q_yy)}\right]dxdy \\
& +\frac{C_{11}}{2L_xL_y}\int_0^{L_y}\int_0^{L_x}\tilde{\epsilon}_{zz}\left(x,y,z_{\mathrm{m}}\right)\left[\sum_{q_x,-q_x}\sum_{q_y,-q_y}\tilde{u}_z\left(q_x,q_y,z_{\mathrm{m}}\right)e^{\mathrm{i}(q_xx+q_yy)}\right]dxdy
\end{aligned}
\tag{3.15}
$$

Solving the above equation in a similar manner to the 2-D case mentioned in the section 3.2, we arrive at the following expression

$$
\begin{aligned}
U_{\mathrm{el}}(\mathbf{q}) = \sum_q & \left[\begin{array}{ccc}\tilde{u}_x\left(-q_x,-q_y,z_{\mathrm{m}}\right) & \tilde{u}_y\left(-q_x,-q_y,z_{\mathrm{m}}\right) & \tilde{u}_z\left(-q_x,-q_y,z_{\mathrm{m}}\right)\end{array}\right]\left[\begin{array}{c}\mathrm{M}_{ij}^{(1)}\end{array}\right]\left[\begin{array}{c}\tilde{u}_x\left(q_x,q_y,z_{\mathrm{m}}\right)\\ \tilde{u}_y\left(q_x,q_y,z_{\mathrm{m}}\right)\\ \tilde{u}_z\left(q_x,q_y,z_{\mathrm{m}}\right)\end{array}\right] \\
& +\left[\begin{array}{ccc}\tilde{u}_x\left(-q_x,q_y,z_{\mathrm{m}}\right) & \tilde{u}_y\left(-q_x,q_y,z_{\mathrm{m}}\right) & \tilde{u}_z\left(-q_x,q_y,z_{\mathrm{m}}\right)\end{array}\right]\left[\begin{array}{c}\mathrm{M}_{ij}^{(2)}\end{array}\right]\left[\begin{array}{c}\tilde{u}_x\left(q_x,-q_y,z_{\mathrm{m}}\right)\\ \tilde{u}_y\left(q_x,-q_y,z_{\mathrm{m}}\right)\\ \tilde{u}_z\left(q_x,-q_y,z_{\mathrm{m}}\right)\end{array}\right],
\end{aligned}
\tag{3.16}
$$

Where, M_{ij}^{1} and M_{ij}^{2} are the inverse of the Green's function matrices, and have the following form

$$
\begin{aligned}
\mathrm{M}_{ij}^{(1)} &= \left[\begin{array}{ccc}M_{xx}\left(q_x,q_y,z_{\mathrm{m}}\right) & M_{xy}\left(q_x,q_y,z_{\mathrm{m}}\right) & iM_{xz}\left(q_x,q_y,z_{\mathrm{m}}\right)\\ M_{xy}\left(q_x,q_y,z_{\mathrm{m}}\right) & M_{yy}\left(q_x,q_y,z_{\mathrm{m}}\right) & iM_{yz}\left(q_x,q_y,z_{\mathrm{m}}\right)\\ -iM_{xz}\left(q_x,q_y,z_{\mathrm{m}}\right) & -iM_{yz}\left(q_x,q_y,z_{\mathrm{m}}\right) & M_{zz}\left(q_x,q_y,z_{\mathrm{m}}\right)\end{array}\right], \\
\mathrm{M}_{ij}^{(2)} &= \left[\begin{array}{ccc}M_{xx}\left(q_x,q_y,z_{\mathrm{m}}\right) & -M_{xy}\left(q_x,q_y,z_{\mathrm{m}}\right) & M_{xz}\left(q_x,q_y,z_{\mathrm{m}}\right)\\ -M_{xy}\left(q_x,q_y,z_{\mathrm{m}}\right) & M_{yy}\left(q_x,q_y,z_{\mathrm{m}}\right) & -iM_{yz}\left(q_x,q_y,z_{\mathrm{m}}\right)\\ -iM_{xz}\left(q_x,q_y,z_{\mathrm{m}}\right) & iM_{yz}\left(q_x,q_y,z_{\mathrm{m}}\right) & M_{zz}\left(q_x,q_y,z_{\mathrm{m}}\right)\end{array}\right],
\end{aligned}
\tag{3.17}
$$

Here,

$$
\begin{aligned}
M_{xx}(q_x,q_y,z_{\mathrm{m}}) &= \frac{2C_{44}\left[4q_x^4(s-1)z_{\mathrm{m}}+q_{\mathrm{r}}q_y^2\coth\left(q_{\mathrm{r}}z_{\mathrm{m}}\right)\left[2(s+1)^2\sinh^2\left(q_{\mathrm{r}}z_{\mathrm{m}}\right)-2q_y^2(s-1)^2z_{\mathrm{m}}^2\right]\right]}{\left[q_x^2+q_y^2\right]\left[(s+1)^2\sinh^2\left(q_{\mathrm{r}}z_{\mathrm{m}}\right)-q_{\mathrm{r}}^2(s-1)^2z_{\mathrm{m}}^2\right]}\\
&+\frac{4C_{44}q_x^2\left[q_{\mathrm{r}}(s+1)\sinh\left(2q_{\mathrm{r}}z_{\mathrm{m}}\right)-q_y^2(s-1)z_{\mathrm{m}}\left[q_{\mathrm{r}}(s-1)z_{\mathrm{m}}\coth\left(q_{\mathrm{r}}z_{\mathrm{m}}\right)-2\right]\right]}{\left[q_x^2+q_y^2\right]\left[(s+1)^2\sinh^2\left(q_{\mathrm{r}}z_{\mathrm{m}}\right)-q_{\mathrm{r}}^2(s-1)^2z_{\mathrm{m}}^2\right]}\\
M_{xy}(q_x,q_y,z_{\mathrm{m}}) &= \frac{2C_{44}q_xq_y[1-s]\left[2q_{\mathrm{r}}z_{\mathrm{m}}(q_{\mathrm{r}}(s-1)z_{\mathrm{m}}\coth\left(q_{\mathrm{r}}z_{\mathrm{m}}\right)+2)-(s+1)\sinh\left(2q_{\mathrm{r}}z_{\mathrm{m}}\right)\right]}{8q_{\mathrm{r}}\left[q_{\mathrm{r}}^2(s-1)^2z_{\mathrm{m}}^2-(s+1)^2\sinh^2\left(q_{\mathrm{r}}z_{\mathrm{m}}\right)\right]}\\
M_{xz}(q_x,q_y,z_{\mathrm{m}}) &= -\frac{i2q_x\left[(C_{11}-C_{12}+2C_{44})q_{\mathrm{r}}^2(s-1)^2z_{\mathrm{m}}^2\right]}{8\left[(s+1)^2\sinh^2\left(q_{\mathrm{r}}z_{\mathrm{m}}\right)-q_{\mathrm{r}}^2(s-1)^2z_{\mathrm{m}}^2\right]}\\
&+\frac{\left[(s+1)(C_{11}(s-1)+C_{12}(s+1)-2C_{44}s)\sinh^2\left(q_{\mathrm{r}}z_{\mathrm{m}}\right)\right]}{8\left[(s+1)^2\sinh^2\left(q_{\mathrm{r}}z_{\mathrm{m}}\right)-q_{\mathrm{r}}^2(s-1)^2z_{\mathrm{m}}^2\right]}
\end{aligned}
$$

$$
\begin{aligned}
M_{yy}(q_x,q_y,z_{\mathrm{m}}) &= -\frac{2C_{44}\left[2q_x^4q_{\mathrm{r}}(s-1)^2z_{\mathrm{m}}^2\coth\left(q_{\mathrm{r}}z_{\mathrm{m}}\right)-2q_y^2(2q_y^2(s-1)z_{\mathrm{m}}+q_{\mathrm{r}}(s+1)\sinh\left(2q_{\mathrm{r}}z_{\mathrm{m}}\right))\right]}{\left[q_x^2+q_y^2\right]\left[(s+1)^2\sinh^2\left(q_{\mathrm{r}}z_{\mathrm{m}}\right)-q_{\mathrm{r}}^2(s-1)^2z_{\mathrm{m}}^2\right]}\\
&-\frac{2C_{44}q_x^2\left[2q_y^2(s-1)z_{\mathrm{m}}(q_{\mathrm{r}}(s-1)z_{\mathrm{m}}\coth\left(q_{\mathrm{r}}z_{\mathrm{m}}\right)-2)-q_{\mathrm{r}}(s+1)^2\sinh\left(2q_{\mathrm{r}}z_{\mathrm{m}}\right)\right]}{\left[q_x^2+q_y^2\right]\left[(s+1)^2\sinh^2\left(q_{\mathrm{r}}z_{\mathrm{m}}\right)-q_{\mathrm{r}}^2(s-1)^2z_{\mathrm{m}}^2\right]}\\
M_{yz}(q_x,q_y,z_{\mathrm{m}}) &= -\frac{i2q_y\left[(C_{11}-C_{12}+2C_{44})\,q_{\mathrm{r}}^2(s-1)^2z_{\mathrm{m}}^2\right]}{8\left[(s+1)^2\sinh^2\left(q_{\mathrm{r}}z_{\mathrm{m}}\right)-q_{\mathrm{r}}^2(s-1)^2z_{\mathrm{m}}^2\right]}\\
&+\frac{\left[(s+1)\left(C_{11}(s-1)+C_{12}(s+1)-2C_{44}s\right)\sinh^2\left(q_{\mathrm{r}}z_{\mathrm{m}}\right)\right]}{8\left[(s+1)^2\sinh^2\left(q_{\mathrm{r}}z_{\mathrm{m}}\right)-q_{\mathrm{r}}^2(s-1)^2z_{\mathrm{m}}^2\right]}\\
M_{zz}(q_x,q_y,z_{\mathrm{m}}) &= -\frac{C_{11}\left[8q_{\mathrm{r}}^2(s-1)sz_{\mathrm{m}}-4q_{\mathrm{r}}s(s+1)\sinh\left(2q_{\mathrm{r}}z_{\mathrm{m}}\right)\right]}{8\left[(s+1)^2\sinh^2\left(q_{\mathrm{r}}z_{\mathrm{m}}\right)-q_{\mathrm{r}}^2(s-1)^2z_{\mathrm{m}}^2\right]}
\end{aligned}
\tag{3.18}
$$

3.5 Asymptotic analysis

This section gives the components of the Green's function matrix for two limiting cases namely for the long wavevector limit and for short wavevector limit. Here, we verify the correctness of the 3-D Green's function matrix by comparing it with that of the 2-D case. As $u(x,y,z)$ reduces to a constant when $q_x = 0$ and $q_y = 0$ (Tab. 3.1), the short wavevector limit ($q_x z_{\mathrm{m}} << 0$, $q_y z_{\mathrm{m}} << 0$) corresponds to the case of uniform loading. It can be seen from Table 3.1 that there exists a one-to-one correspondence between the components of the 2-D and 3-D cases. The long wavevector limit ($q_x z_{\mathrm{m}} >> 0$,$q_y z_{\mathrm{m}} >> 0$) corresponds to the case of seminfinite elastic solid. It can be seen from Table 3.3 that the components of the Green's function matrix for a 3-D case reduces to that of a 2-D case when one of the wavevectors is eliminated.

Table 3.1: Components of the Green's function matrix for the short wavevector limit

Short wave vector limit($q_x z_\mathrm{m} << 0, q_y z_\mathrm{m} << 0$)		
M_{ij}	3D	2D
M_{xx}	$\frac{C_{44}}{2z_m}$	$\frac{C_{44}}{2z_m}$
M_{xy}	0	0
M_{xz}	0	0
M_{yy}	$\frac{C_{44}}{2z_m}$	0
M_{yz}	0	0
M_{zz}	$\frac{C_{11}}{2z_m}$	$\frac{C_{11}}{2z_m}$

Table 3.2: Components of the Green's function matrix for the case of long wavevector limit

Long wave vector limit($q_x z_\mathrm{m} >> 0, q_y z_\mathrm{m} >> 0$)		
M_{ij}	3D	2D
M_{xx}	$\frac{C_{44}\left(q_y^2(s+1)+2q_x^2\right)}{2\sqrt{q_x^2+q_y^2}(s+1)}$	$\frac{qC_{44}}{1+s}$
M_{xy}	$-\frac{C_{44}q_xq_y(s-1)}{2\sqrt{q_x^2+q_y^2}(s+1)}$	0
M_{xz}	$\frac{C_{44}q_xs}{(s+1)}$	$\frac{qsC_{44}}{1+s}$
M_{yy}	$\frac{C_{44}\left(q_x^2(s+1)+2q_y^2\right)}{2\sqrt{q_x^2+q_y^2}(s+1)}$	0
M_{yz}	$\frac{C_{44}q_ys}{s+1}$	0
M_{zz}	$\frac{C_{11}\sqrt{q_x^2+q_y^2}s}{s+1}$	$\frac{qC_{44}}{1+s}$

As expected, when one of the wavevectors is made equal to zero, the analytical solution of the displacement for a 3-D boundary value problem given by equation 4.10 reduces to that of the corresponding 2-D plane strain boundary value problem. Fig. 3.9 shows the schematic of the above described boundary value problem. Figures 3.10 and 3.11 compare the displacement fields of the 3-D and 2-D cases. It can be seen that there exists a one-to-one correspondence between the two.

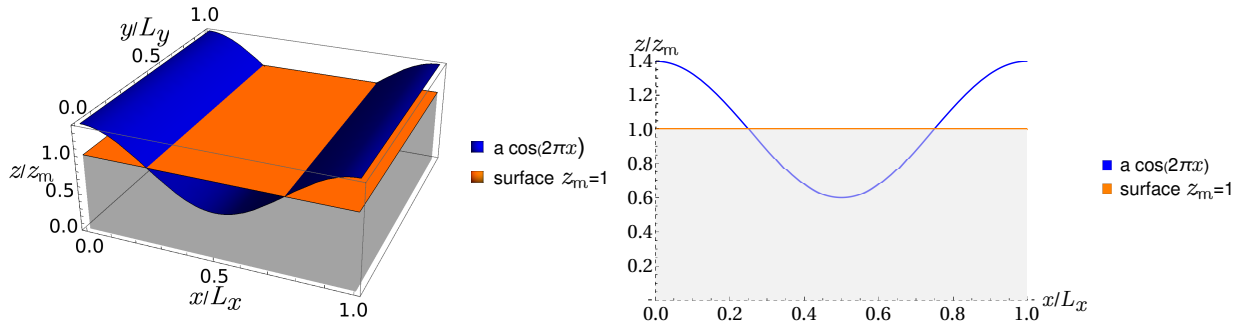

(a) (b)

Figure 3.9: Cosinusoidal loading on a) 3-D solid, b) 2-D solid.

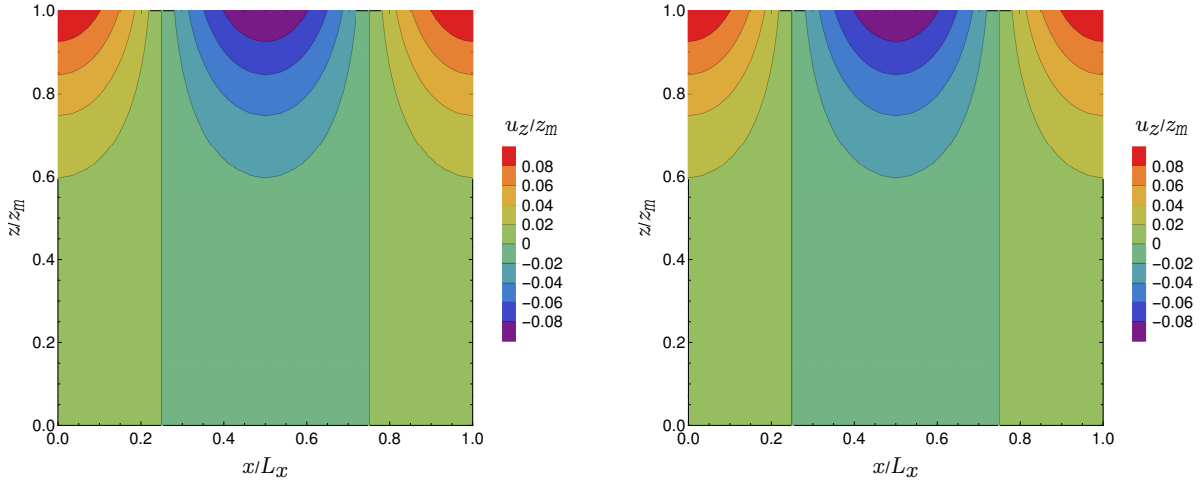

(a) (b)

Figure 3.10: Normal displacement Calculated using a) 3-D analytical solution, b) 2-D analytical solution.

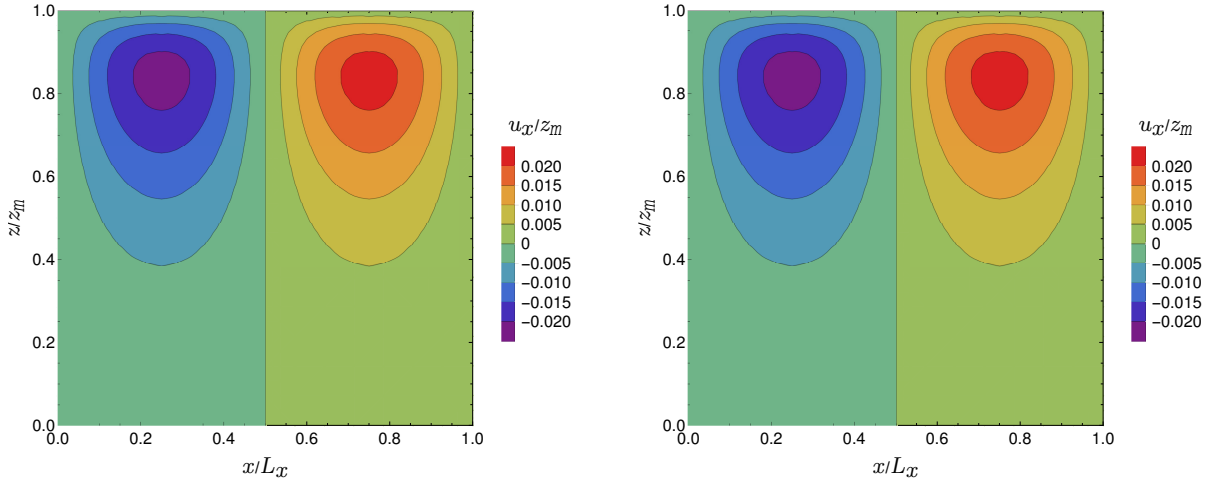

(a) (b)

Figure 3.11: Lateral displacement Calculated using a) 3-D analytical solution, b) 2-D analytical solution.

Table 3.3: Components of the Green's function matrix

M_{ij}	3D when $q_y = 0$	2D
M_{xx}	$\frac{C_{11}q[1-r]\left[\sinh\left(qz_{\mathrm{m}}\right)\cosh\left(qz_{\mathrm{m}}\right)-rqz_{\mathrm{m}}\right]}{2\left[-r^2qz_{\mathrm{m}}^2+\cosh^2\left(qz_{\mathrm{m}}\right)-1\right]}$	$\frac{C_{11}q[1-r]\left[\sinh\left(qz_{\mathrm{m}}\right)\cosh\left(qz_{\mathrm{m}}\right)-rqz_{\mathrm{m}}\right]}{2\left[-r^2qz_{\mathrm{m}}^2+\cosh^2\left(qz_{\mathrm{m}}\right)-1\right]}$
M_{xy}	0	0
M_{xz}	$\frac{C_{11}q[1-r]\left[(1-r)\sinh^2\left(qz_{\mathrm{m}}\right)-2r^2qz_{\mathrm{m}}^2\right]}{2[r+1]\left[-r^2qz_{\mathrm{m}}^2+\cosh^2\left(qz_{\mathrm{m}}\right)-1\right]}$	$\frac{C_{11}q[1-r]\left[(1-r)\sinh^2\left(qz_{\mathrm{m}}\right)-2r^2qz_{\mathrm{m}}^2\right]}{2[r+1]\left[-r^2qz_{\mathrm{m}}^2+\cosh^2\left(qz_{\mathrm{m}}\right)-1\right]}$
M_{yy}	$\frac{C_{44}\sqrt{q_x^2}\coth\left(\sqrt{q_x^2}z_m\right)}{2}$	0
M_{yz}	0	0
M_{zz}	$\frac{C_{11}q[1-r]\left[rqz_{\mathrm{m}}+\sinh\left(qz_{\mathrm{m}}\right)\cosh\left(qz_{\mathrm{m}}\right)\right]}{2\left[-r^2qz_{\mathrm{m}}^2+\cosh^2\left(qz_{\mathrm{m}}\right)-1\right]}$	$\frac{C_{11}q[1-r]\left[rqz_{\mathrm{m}}+\sinh\left(qz_{\mathrm{m}}\right)\cosh\left(qz_{\mathrm{m}}\right)\right]}{2\left[-r^2qz_{\mathrm{m}}^2+\cosh^2\left(qz_{\mathrm{m}}\right)-1\right]}$

Chapter 4

Indentation by an array of flat rigid punches

4.1 Introduction

In the previous chapter we derived the analytical solution to the Green's function matrix. We verified the correctness of the Green's function matrix by comparing its limits with the 2-D Green's function matrix under special cases. Here, in this chapter we verify the dynamically equilibrated solution by comparing the GFMD results with FEM results for the indentation of an elastic slab by a periodic array of flat rigid punches.

The damping factor used in the dynamics for the hardwall interaction strongly influences the time taken for the system to equilibrate. This effect can be seen in the numerical results of the simulation involving the indentation of a 3-D linear elastic solid by a flat rigid punch. Fig. 4.1 shows the dynamic Fourier amplitude of the slowest mode as a function of the iteration step and it can be seen that for the same number of total iteration steps (n_{tot}), the system which is critically damped converges faster to the exact solution. To obtain a fast equilibration we used the critical damping factor of the slowest mode to damp all the harmonic modes in the GFMD simulations. Recently mode dependent critical damping factors were derived analytically by Dokkum *et al.* [11] and as described in the following section.

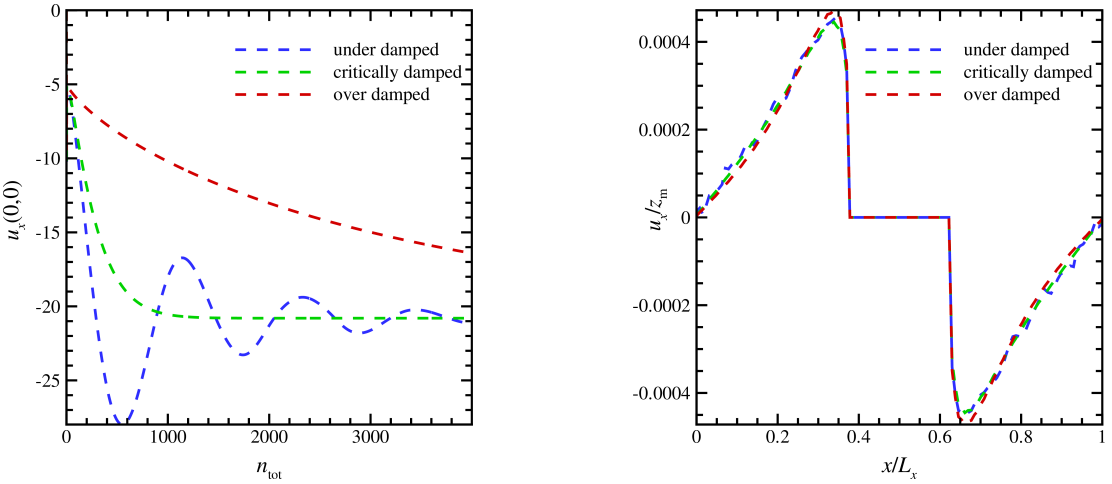

(a) (b)

Figure 4.1: Convergence of the solution as a function of damping factors a) $\tilde{u_x}(0,0)$, b) $\frac{u_x}{z_{\mathrm{m}}}(\frac{x}{L_x}, \frac{y}{L_y} = 0.5, \frac{z}{z_{\mathrm{m}}})$.

4.2 Determination of the critical damping factor

Here, we adopt the methodology used by Dokkum *et al.* [11] to determine the damping factors corresponding to the different characteristic dynamic regimes of a damped harmonic oscillator. We start with writing the pSV equations in its velocity explicit and position explicit scheme

$$\tilde{\boldsymbol{v}}_{n+1}(\mathbf{q}) = \tilde{\boldsymbol{P}}_n^{\mathrm{el}}(\Delta t) - \tilde{v}_n(1 - \eta(\Delta t^2)) \tag{4.1}$$

$$\tilde{\boldsymbol{u}}_{n+1}(\mathbf{q}) = \tilde{u}_n(\mathbf{q}) + \tilde{\boldsymbol{P}}_n^{\mathrm{el}}(\Delta t)^2 - \tilde{v}_n(\Delta t - \eta(\Delta t^3)) \tag{4.2}$$

as a matrix difference equation in general form

$$\begin{bmatrix} \tilde{\boldsymbol{u}}_{n+1}(\mathbf{q}) \\ \tilde{\boldsymbol{v}}_{n+1}(\mathbf{q}) \end{bmatrix} = \begin{bmatrix} \vartheta \end{bmatrix} \begin{bmatrix} \tilde{\boldsymbol{u}}_{n}(\mathbf{q}) \\ \tilde{\boldsymbol{v}}_{n}(\mathbf{q}) \end{bmatrix}. \tag{4.3}$$

Extending to the 3-D case results in the following matrix ϑ

$$\vartheta = \begin{bmatrix} 1+M_{11}(\Delta t)^2 & M_{12}(\Delta t)^2 & M_{13}(\Delta t)^2 & \Delta t-\eta_1(\Delta t^3)0 & 0 & \\ M_{12}(\Delta t)^2 & 1+M_{22}(\Delta t)^2 & M_{23}(\Delta t)^2 & 0 & \Delta t-\eta_2(\Delta t^3) & 0 \\ M_{13}(\Delta t)^2 & M_{23}(\Delta t)^2 & 1+M_{33}(\Delta t)^2 & 0 & 0 & \Delta t-\eta_3(\Delta t^3) \\ M_{11}(\Delta t) & M_{12}(\Delta t) & M_{13}(\Delta t) & 1-\eta_1(\Delta t^2) & 0 & 0 \\ M_{12}(\Delta t) & M_{22}(\Delta t) & M_{23}(\Delta t) & 0 & 1-\eta_2(\Delta t^2) & 0 \\ M_{13}(\Delta t) & M_{23}(\Delta t) & M_{33}(\Delta t) & 0 & 0 & 1-\eta_3(\Delta t^2) \end{bmatrix}. \tag{4.4}$$

where M_{ij} correspond to the components of the Green's function matrix derived in Sec. 3.4. η_i is the direction specific damping factor. The different dynamic characteristic regimes of the damped harmonic oscillator are given by the eigen values of the matrix. The critical damping factor for each of the modes can be obtained by equating the eigen values of the matrix to each other. Moreover, it was shown by Dokkum *et al.* that the first harmonic mode $\tilde{u}(0,0)$ is the slowest mode and applying the results of the limits of the Green's function matrix as given in the Sec. 3.5, we get the following

$$\eta_{i,\mathrm{cr}}(\mathbf{q}=0,z_{\mathrm{m}}) = 2\frac{\sqrt{\kappa_i}}{\Delta t} - \kappa_i, \tag{4.5}$$

$$\kappa_1(\mathbf{q}=0,z_{\mathrm{m}}) = \frac{C_{44}}{z_{\mathrm{m}}}, \kappa_2(\mathbf{q}=0,z_{\mathrm{m}}) = \frac{C_{44}}{z_{\mathrm{m}}}, \kappa_3(\mathbf{q}=0,z_{\mathrm{m}}) = \frac{C_{11}}{z_{\mathrm{m}}} \tag{4.6}$$

Dependency of the critical damping factor on the material properties, substrate geometry, interfacial properties and the discrete time−step Δt can be seen from the above equations. We use the damping factor of the slowest mode to damp all the other modes. The equilibration of the harmonic modes are collectively verified by validating the GFMD simulation results with the FEM results.

4.3 Numerical simulation of the indentation problems

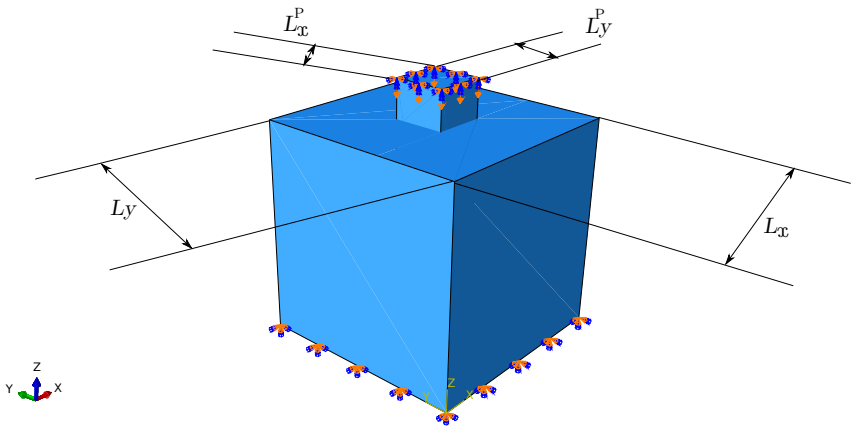

Figure 4.2: Schematic representation of the indentation of a unit cell by a flat rigid punch.

The boundary value problem shown in the Fig. 4.2 is solved by the GFMD technique using the 3-D Green's function matrix derived in Sec. 3.4. The GFMD simulation is performed in a periodic unit cell with fixed bottom, where L_x and L_y are the length and width of the unit cell being equal to 1.27 μm. The ratio $L_x^{\mathrm{p}}/L_x = L_y^{\mathrm{p}}/L_y$ of the slab to punch is 0.25, where L_x^{p} and L_y^{p} are the length and width of the punch respectively. Contact between the flat rigid punch and the slab is assumed to be fully sticking with the following constraints imposed:

$$\begin{array}{l} u_z(x,y,z_{\mathrm{m}}) = u_z^0, \\ u_y(x,y,z_{\mathrm{m}}) = 0, \\ u_x(x,y,z_{\mathrm{m}}) = 0, \end{array} \qquad \text{for} \quad \frac{L_x - L_x^{\mathrm{p}}}{2} < x < \frac{L_x + L_x^{\mathrm{p}}}{2} \text{ and } \frac{L_y - L_y^{\mathrm{p}}}{2} < y < \frac{L_y + L_y^{\mathrm{p}}}{2}, \tag{4.7}$$

where u_z^0 the displacement prescribed at the top surface is 0.005 μm. Outside the contact region, the surface is assumed to be traction free. The slab is assumed to have the elastic properties of aluminum with young's modulus E= 70 GPa, Poisson's ratio $\nu = 0.33$ and $s = \dfrac{C_{44}}{C_{11}} = 0.25$. For the GFMD simulation the surface is discretized using $nx \times ny$ equispaced grid points, with nx=128 and ny=128. Contact between the rigid indenters and the slab is modeled through a hard-wall condition. The damping factor $\eta_{1,\mathrm{cr}}$ used in the simulations is given by

$$\eta_{1,\mathrm{cr}}(\mathbf{q} = 0, z_{\mathrm{m}}) = 2\frac{\sqrt{\kappa_1}}{\Delta t} - \kappa_1, \tag{4.8}$$

$$\kappa_1(\mathbf{q} = 0, z_{\mathrm{m}}) = \frac{C_{44}}{z_{\mathrm{m}}}, \tag{4.9}$$

where Δt the time step = 0.25.

Fig. 4.3a, 4.4a, 4.5a shows the displacement fields at the surface u_x, u_y ,u_z which are obtained by the damped dynamic energy minimization. The corresponding displacement fields calculated by FEM are shown in the Fig. 4.3b, 4.4b and 4.5b. Both the above methods have the same discretization nodes of the surface layer.

The variation of the displacements u_x, u_y ,u_z along the height of the solid as shown in Fig. 4.7a, 4.8a, 4.9a is obtained from the analytical solution to Fourier space displacement fields derived in Sec.3.3

$$\begin{bmatrix} \tilde{u}_x(\mathbf{q},z) \\ \tilde{u}_y(\mathbf{q},z) \\ \tilde{u}_z(\mathbf{q},z) \end{bmatrix} = \begin{bmatrix} f_1(q_x,q_y,z) & f_2(q_x,q_y,z) & f_3(q_x,q_y,z) \\ f_2(q_x,q_y,z) & f_4(q_x,q_y,z) & f_5(q_x,q_y,z) \\ f_3(q_x,q_y,z) & f_5(q_x,q_y,z) & f_6(q_x,q_y,z) \end{bmatrix} \begin{bmatrix} a_1 \\ a_2 \\ a_3 \end{bmatrix} \tag{4.10}$$

Detailed expressions of the components f_i are given in Sec.3.3. We later obtain the real space displacement fields using the definition of the inverse Fourier transform

$$\begin{aligned} u_z(x,y,z_{\mathrm{m}}) = \sum_{q_x,q_y} & \tilde{u}_z\left(q_x,q_y,z_{\mathrm{m}}\right) e^{\mathrm{i}(q_x x + q_y y)} + \tilde{u}_z\left(-q_x,-q_y,z_{\mathrm{m}}\right) e^{-\mathrm{i}(q_x x + q_y y)} \\ & + \tilde{u}_z\left(q_x,-q_y,z_{\mathrm{m}}\right) e^{\mathrm{i}(q_x x - q_y y)} + \tilde{u}_z\left(-q_x,q_y,z_{\mathrm{m}}\right) e^{-\mathrm{i}(q_x x - q_y y)}. \end{aligned} \tag{4.11}$$

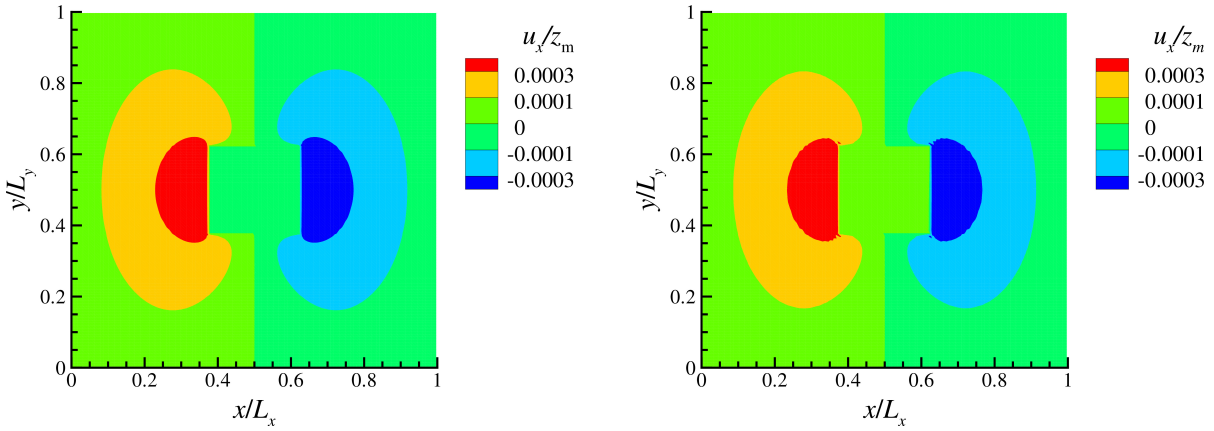

(a) (b)

Figure 4.3: Displacement $\frac{u_x}{z_m}(\frac{x}{L_x}, \frac{y}{L_y}, \frac{z}{z_m} = 1)$ calculated by GFMD a) calculated by FEM.

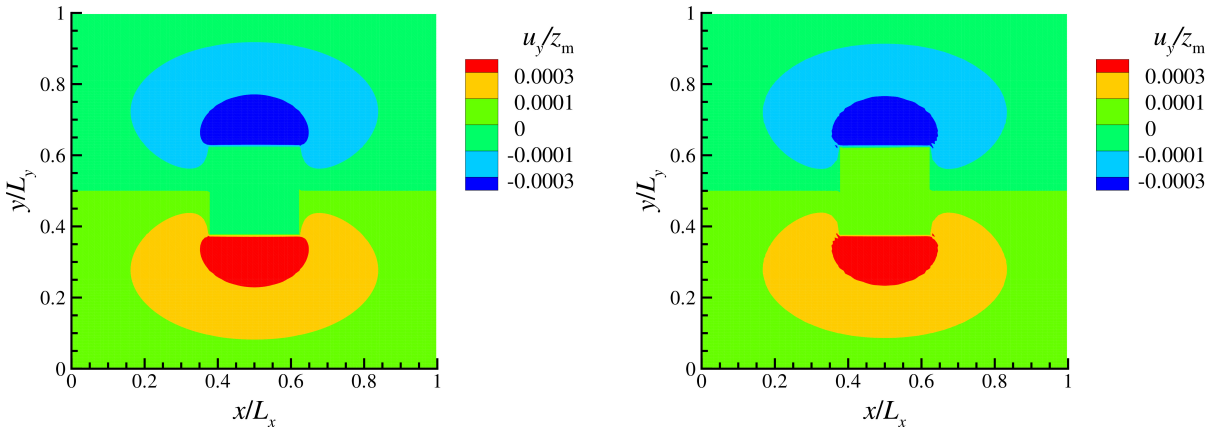

(a) (b)

Figure 4.4: Displacement $\frac{u_y}{z_m}(\frac{x}{L_x}, \frac{y}{L_y}, \frac{z}{z_m} = 1)$ calculated by GFMD a) calculated by FEM.

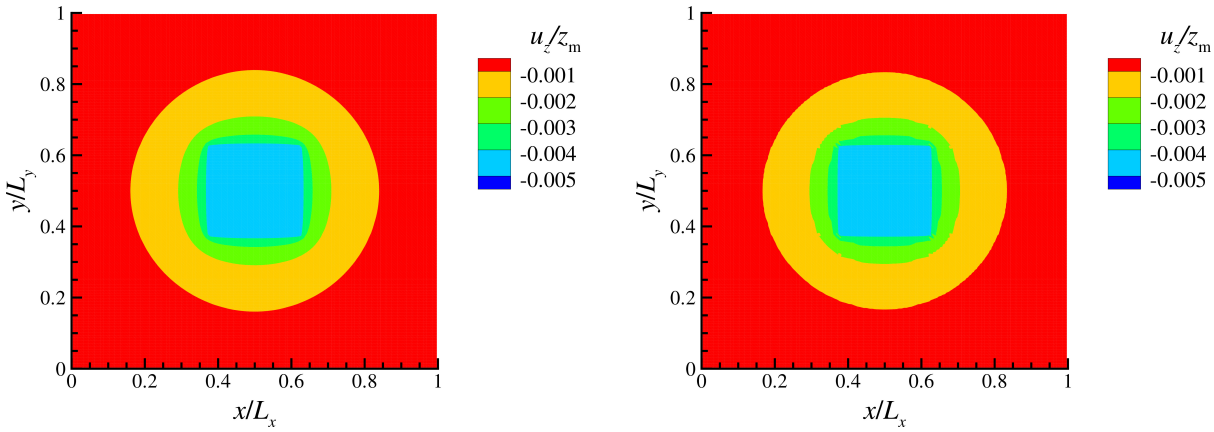

(a) (b)

Figure 4.5: Displacement $\frac{u_z}{z_m}(\frac{x}{L_x}, \frac{y}{L_y}, \frac{z}{z_m} = 1)$ calculated by GFMD a) calculated by FEM.

From the Fourier space displacements we can calculate the Fourier space stress fields from the corresponding stress-strain relations of a linear elastic solid

$$\begin{bmatrix} \tilde{\sigma}_x(\mathbf{q},z) \\ \tilde{\sigma}_y(\mathbf{q},z) \\ \tilde{\sigma}_z(\mathbf{q},z) \\ \tilde{\sigma}_{xy}(\mathbf{q},z) \\ \tilde{\sigma}_{yz}(\mathbf{q},z) \\ \tilde{\sigma}_{zx}(\mathbf{q},z) \end{bmatrix} = \begin{bmatrix} C_{11} & C_{12} & C_{12} & 0 & 0 & 0 \\ C_{12} & C_{11} & C_{12} & 0 & 0 & 0 \\ C_{12} & C_{12} & C_{11} & 0 & 0 & 0 \\ 0 & 0 & 0 & C_{44} & 0 & 0 \\ 0 & 0 & 0 & 0 & C_{44} & 0 \\ 0 & 0 & 0 & 0 & 0 & C_{44} \end{bmatrix} \begin{bmatrix} \tilde{\epsilon}_{xx}(\mathbf{q},z) \\ \tilde{\epsilon}_{yy}(\mathbf{q},z) \\ \tilde{\epsilon}_{zz}(\mathbf{q},z) \\ \tilde{\epsilon}_{xy} \\ \tilde{\epsilon}_{yz} \\ \tilde{\epsilon}_{zx} \end{bmatrix},$$

$$\begin{bmatrix} \tilde{\epsilon}_{xx}(\mathbf{q},z) \\ \tilde{\epsilon}_{yy}(\mathbf{q},z) \\ \tilde{\epsilon}_{zz}(\mathbf{q},z) \\ \tilde{\epsilon}_{xy} \\ \tilde{\epsilon}_{yz} \\ \tilde{\epsilon}_{zx} \end{bmatrix} = \begin{bmatrix} (iq_x)\tilde{u}_x(\mathbf{q},z) \\ (iq_y)\tilde{u}_y(\mathbf{q},z) \\ \dfrac{\partial u_z(\mathbf{q},z)}{\partial z} \\ (iq_y)\tilde{u}_x(\mathbf{q},z) + (iq_x)\tilde{u}_y(\mathbf{q},z) \\ \dfrac{\partial u_x(\mathbf{q},z)}{\partial z} + (iq_x)\tilde{u}_z(\mathbf{q},z) \\ \dfrac{\partial u_y(\mathbf{q},z)}{\partial z} + (iq_y)\tilde{u}_z(\mathbf{q},z) \end{bmatrix} \tag{4.12}$$

The real space stress fields shown in the Figure are then obtained by a similar manner shown in the equation 4.11.

The error between the two numerical results (FEM and GFMD),

$$err_{\text{GFMD}} = \frac{\sqrt{< (u_x^{\text{FEM}} - u_x^{\text{GFMD}})^2 >}}{u_z^0} \tag{4.13}$$

in Fig. 4.6 is ≈ 0.00196. This error can be minimized with mesh refinements in the case of both GFMD and FEM.

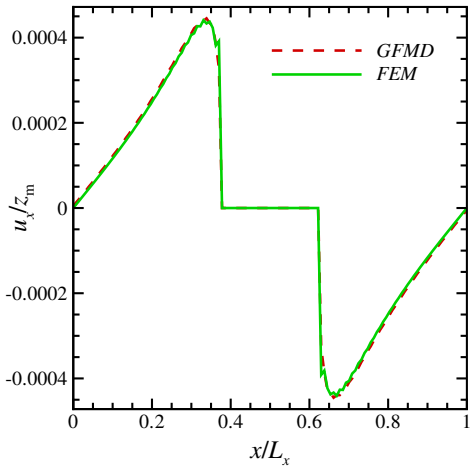

Figure 4.6: Comparison of the displacements obtained by GFMD and FEM $\frac{u_x}{z_{\text{m}}}(\frac{x}{L_x}, \frac{y}{L_y} = 0.5, \frac{z}{z_{\text{m}}})$

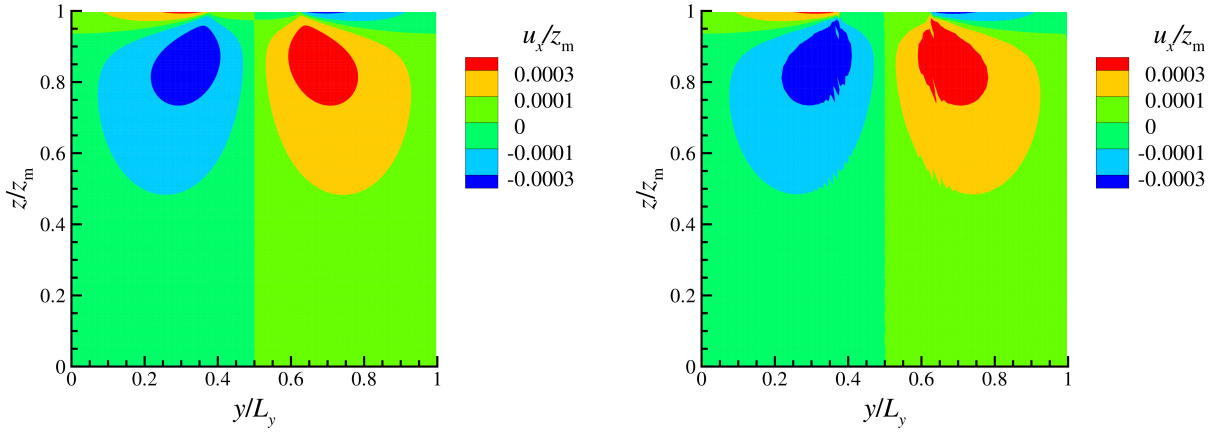

Figure 4.7: Displacement $\frac{u_x}{z_m}(\frac{x}{L_x}=0.5,\frac{y}{L_y},\frac{z}{z_m})$ calculated by a) GFMD, b) FEM.

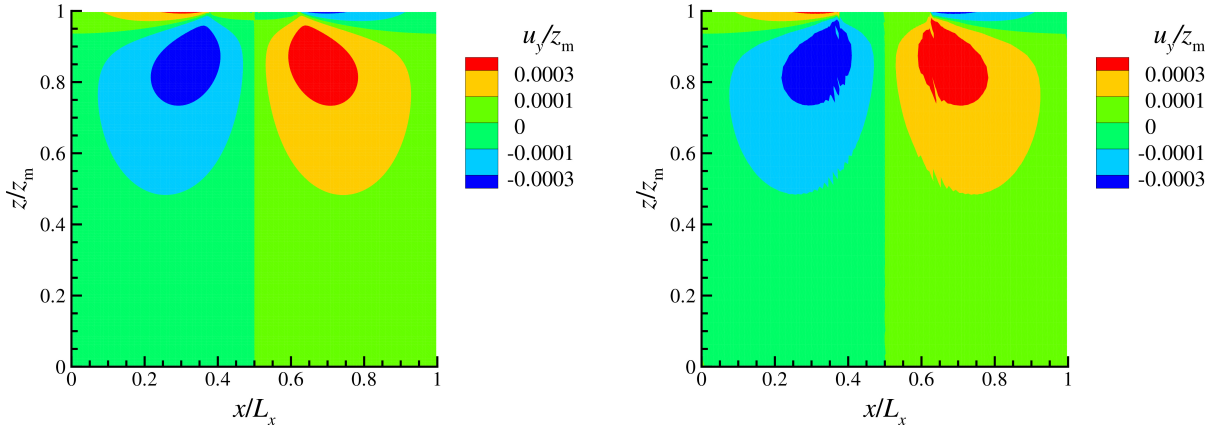

Figure 4.8: Displacement $\frac{u_y}{z_m}(\frac{x}{L_x},\frac{y}{L_y}=0.5,\frac{z}{z_m})$ calculated by a) GFMD, b) FEM.

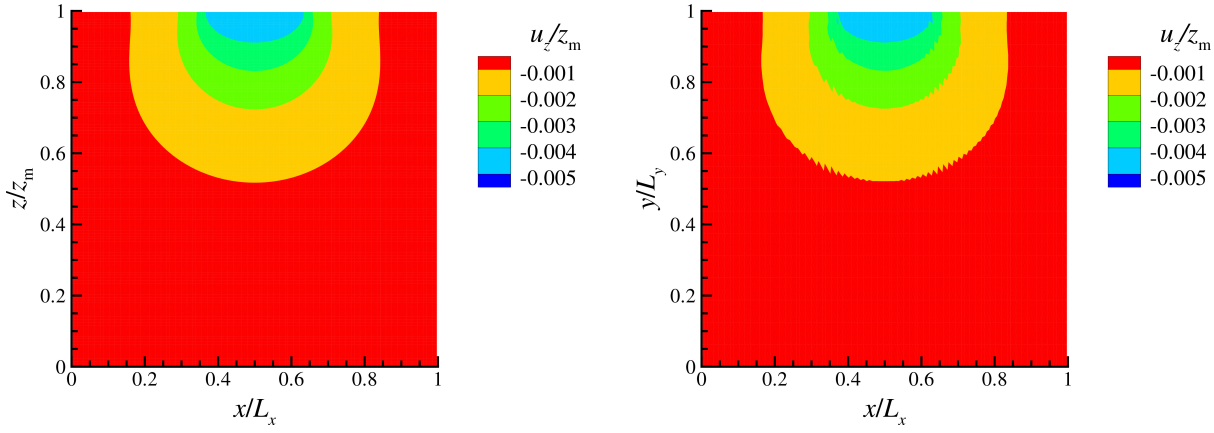

Figure 4.9: Displacement $\frac{u_z}{z_m}(\frac{x}{L_x}=0.5,\frac{y}{L_y},\frac{z}{z_m})$ calculated by a) GFMD, b) FEM.

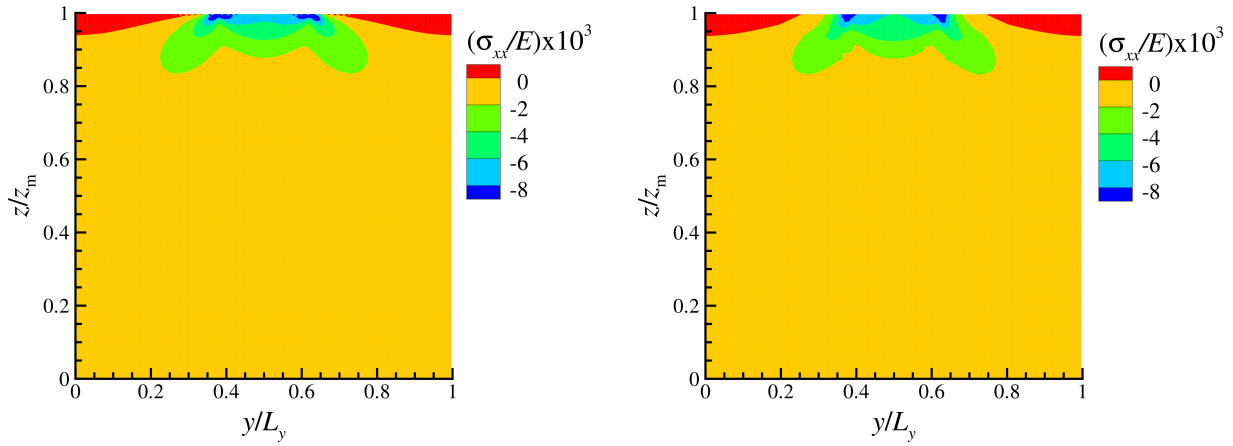

(a) (b)

Figure 4.10: Stress $\sigma_{xx}(\frac{x}{L_x} = 0.5, \frac{y}{L_y}, \frac{z}{z_{\mathrm{m}}})$ calculated by a) GFMD, b) FEM.

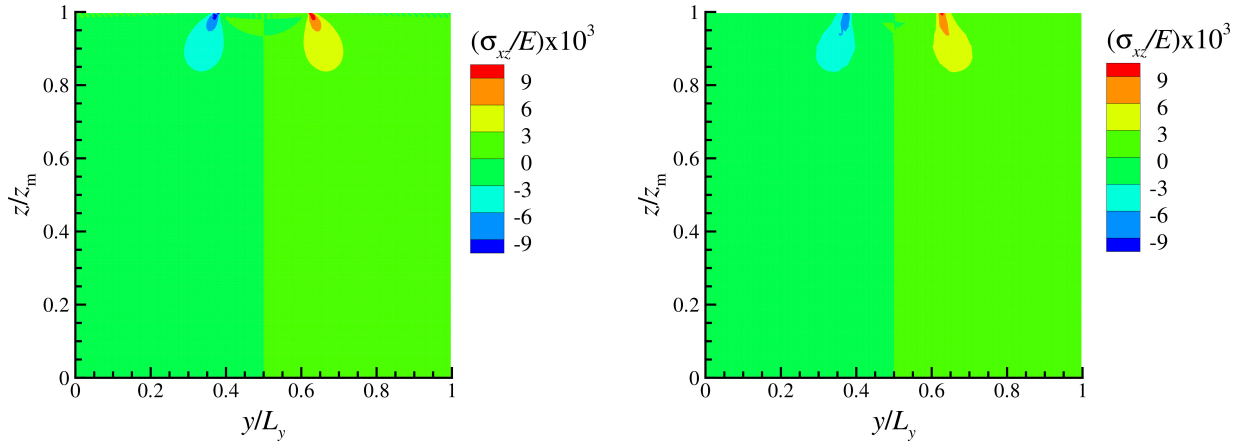

(a) (b)

Figure 4.11: Stress $\sigma_{xz}(\frac{x}{L_x} = 0.5, \frac{y}{L_y}, \frac{z}{z_{\mathrm{m}}})$ calculated by a) GFMD, b) FEM.

Chapter 5

Estimation of the proportionality between area and load

5.1 Introduction

In this chapter we analyse the numerically determined the proportionality constant κ for the indentation of an elastic slab with a flat surface by a rough rigid indenter having self affine rough surface, through comparison with other analytical models.

Previous studies on κ determination by various authors are summarized in the following Table

Authors	H	κ	ϵ_c^{-1}	ϵ_f^{-1}	ϵ_t^{-1}	a	$\kappa = f(x)$
Bush *et al.* [7]	0...1	$\sqrt{8/\pi}...\sqrt{2\pi}$	0	≈ 1	0	∞	H
Persson [22]	0...1	$\sqrt{8/\pi}$	0	0	0	∞	-
Hyun *et al.* [8]	0.3...0.9	2.2...1.8	2	≈ 1000	1	1	ν, H
Campañá *et al.* [16]	0.2...0.8	2.09...1.98	ext.	≈ 1000	1	∞	H
Prodanov *et al.* [3]	0...0.8	2.16...1.93	ext.	ext.	ext.	∞	-
Dokkum *et al.* [11]	0...0.8	1.45	ext.	ext.	ext.	$0.5, 1, 4, \infty$	H,ν,a
Yastrebov *et al.* [23]	0...0.8	2.4...2.2	0	32...512	0	1	H

Table 5.1: The values of κ at $\bar{p}/E^* \approx 0.1$ obtained by different authors. The term "$\kappa = f(x)$" indicates the observed dependency of the value of κ, "ext." means extrapolation to the corresponding limit, i.e., $\epsilon_i \to 0^+$.

Bush *et al.* [7] reported the value of κ in the continuum and thermodynamic limit. The authors modelled the rough surface as uncorrelated individual non-spherical asperities having a statistical distribution of heights and radii of curvature. Therefore, their theory is limited to the description of roughness on a single length scale. Neglecting the interaction between the individual asperities lead to a over estimation of κ in comparison to the other models.

Persson [22] in his theory computes the broadening of the pressure distribution through the Fourier integral, thereby inherently preventing the finite thermodynamic, fractal and continuum discretizations of the system. The theory is accurate for full contact conditions as suggested by the experiments and predicts that the κ is independent of the Hurst exponent.

Pradanov *et al.* [3] used the GFMD to numerically compute the (κ^{sim}) for the contact of an incompressible semi-infinite linear elastic solid and rough rigid indenter with self affine rough surface. The κ^{sim} value is then corrected for the effect of discretizing the system. The authors reported a weak dependence of the κ value to the thermodynamic correction and also reported the κ value to be independent of the Hurst exponent.

Dokkum *et al.* [11] used the extended GFMD by Venugopalan *et al.* [10] to determine the effect of height z_m and Poisson's ratio on the κ^{TFC} value. The continuum limit κ^{TFC} was estimated by adopting the same methodology of Pradanov *et al.* [3]. A negligible dependence of the κ value on the elastic properties and surface topography i.e., E, ν and $\bar{g}$ was reported.

Hyun *et al.* [8] used an FEM model in plane strain, and reported $1.8 \leq \kappa \leq 2.2$ for the finite-height slab with $a = 1$ and Poisson's ratios $0 \leq \nu \leq 0.5$. They observe that the proportionality coeffi- cient κ is dependent on the Hurst exponent H. Moreover, they report that the proportionality coefficient has a higher-order dependency on the Poissons ratio ν. They choose ϵ_c^{-1} and vary $\epsilon_f^{-1} \leq 1000$.

Yastrebov *et al.* [23] focussed only on the continuum limit corrections and analysed the role of roughness length scales (spectral width) on the elastic contact of rough surfaces. The authors reported that the inclusion of small length scale roughness leads to the convergence of the κ value to that of the Persson. Additionally they also found that this effect was more pronounced with the decrease in Hurst exponent.

Among the various numerical studies done so far on the determination of the proportionality constant κ, the work of Prodanov *et al.* [3] was the first to report the extrapolated continuum mechanical proportionality constant κ^{TFC}. As the GFMD simulations can only be done in a finitely discretized system, it leads to the discretization of smallest length-scale roughness by a finite lattice parameter a. Therefore the authors recommended that in order to estimate the correct value for κ it is necessary to remove the following numerical effects namely: finite sized repetitive cell effects introduced by the DFFT used in GFMD (also known as thermodynamic correction) and discretization cell effects, a result of discretizing the smallest length scale roughness by a finite lattice parameter (continuum correction). Moreover, the realistic rough surfaces are self affine to atomistic length scales and therefore the effects of using only a finite number of wave-vectors to describe a self affine rough surface was also corrected for. The thermodynamic ϵ_{t}, fractal ϵ_{f} and continuum discretization ϵ_{c} of a system are expressed as

$$\begin{aligned} \epsilon_{\mathrm{t}} &= \frac{q_0}{q_{\mathrm{l}}}, \\ \epsilon_{\mathrm{f}} &= \frac{q_{\mathrm{l}}}{q_{\mathrm{s},H}}, \\ \epsilon_{\mathrm{c}} &= \frac{q_{\mathrm{s},H}}{q_{\mathrm{s}}} \end{aligned} \tag{5.1}$$

Where q_0 is the wave-vector which corresponds to the length scale of the sample. q_{l} , $q_{\mathrm{s},H}$ are the wave-vectors which correspond to the roughness at the largest length scale and smallest length scale. The q_{s} is the wave-vector which corresponds to the lattice parameter of the system. The corrections were done in the following manner: a reference value for the discretizations ϵ_i were chosen, these are $\epsilon_{\mathrm{c}}^{-1} = 2$, $\epsilon_{\mathrm{f}}^{-1} = 1024$ and $\epsilon_{\mathrm{t}}^{-1} = 2$. The continuum discretization is then independently varied over the values $\epsilon_{\mathrm{c}}^{-1} = 1, 2, 4, 8$ and the κ^{sim} was numerically estimated while maintaining the reference values for fractal and thermodynamic discretizations constant. Subsequently the spectral width was varied over the values $\epsilon_{\mathrm{f}}^{-1} = 512, 1024, 2048, 4096$ maintaining the values of thermodynamic and continuum discretizations. Finally the thermodynamic discretization is varied over the values $\epsilon_{\mathrm{t}}^{-1} = 1, 2, 4, 8$, keeping the other two values of the discretizations constant. The final κ^{sim} value of a system which is discretized with ϵ_{t}, ϵ_{f} and ϵ_{c} is averaged out over N numerical simulations which were performed with surfaces having different surface topographies but constant Hurst exponent. The above average values of κ^{sim} are plotted separately as a function of individual discretizations ϵ_i and a power law fit is performed.

5.2 Methodology

We adopted the same methodology of Pradanov *et al.* [3] and Dokkum *et al.* [11] in the determination of the κ^{TFC} of a compressible finite slab. From the previous studies of κ^{TFC} determination done using the GFMD it was shown that the influence of the thermodynamic correction is very minimal and hence we decided to account only for the continuum and fractal corrections. Thus

equation 5.7 reduces to the following form,

$$\kappa^{\mathrm{TFC}}\left(\bar{p}/E^{*}\bar{g}, H\right) = \kappa^{\mathrm{sim}}\left(\bar{p}/E^{*}\bar{g}, \epsilon_{\mathrm{f}}, \epsilon_{\mathrm{c}}\right) - C_{\mathrm{f}}\epsilon_{\mathrm{f}}^{\alpha_{\mathrm{f}}} - C_{\mathrm{c}}\epsilon_{\mathrm{c}}^{\alpha_{\mathrm{c}}}. \tag{5.2}$$

To this end, we chose the following reference values of discretization $\epsilon_{\mathrm{c}}^{-1} = 4$, $\epsilon_{\mathrm{f}}^{-1} = 256$ and $\epsilon_{\mathrm{t}}^{-1} = 2$. Moreover, we determine the values of the correction factors C_{i} and α_{i} corresponding to the individual discretizations ϵ_i by independently varying the ϵ_c^{-1} over 2, 4, 8 and ϵ_f^{-1} over 128, 256, 512 for the system with Hurst exponent H= 0, Poisson's ratio $\nu = 0.33$ and aspect ratio $a = 1$. We used the Poisson's ratio of aluminum $\nu = 0.33$, as most of the engineering metals have Poisson's ratio in the range of 0.25 to 0.35, the aspect ratio a of the system was chosen to be 1 in order to directly compare our numerical results with those of the Dokkum *et al.* [11], as the latter used the 2D-GFMD. Intentionally, Hurst exponent was chosen to be zero in order to have a Gaussian surface. For a Gaussian surface the roughness is usually characterized by shorter wavelengths and the chosen reference value of the continuum discretization $\epsilon_{\mathrm{c}}^{-1} = 4$ that is nearly four times smaller than that suggested by Pradanov *et al.* [3] leads to a insufficient discretization of the surface. Hence, the determined κ value is the maximum limit value.

In the work of Dokkum *et al.* [11], the desired nominal pressure $\bar{p}$ which was calculated as the traction of the first mode i.e., $f_z(\mathbf{q} = 0)$ is iteratively reached. The author starts by imposing arbitrary displacements onto the rigid punch. Depending on the sign of the difference between the numerically estimated value of $\bar{p}$ and its required value, the displacement is either scaled by a factor of 2 or 0.5 and imposed again onto the system. The equilibrium position is then calculated again, and the above steps are repeated until $\bar{p}$ reaches the desired value. Adopting the same methodology will be computationally expensive for our 3-D case.

All the above studies chose low values of $\bar{p}$ ([3]) and estimate the κ^{sim} as the slope of the linear regime of the contact area fraction versus the nominal pressure curve (with linearity spanning over the region of $\bar{p}$ from 0.001 to 0.01). Therefore, we calculate the κ^{sim} value of a system in the linearity regime of a_r versus $\bar{p}$ by applying five steps of displacements whose corresponding $\bar{p}$ value lies in the range of 0.001 to 0.01.

From the studies of Dokkum *et al.* [11] it was seen that the Power spectral density method (PSDM) generates surfaces closer to the experimentally observed ones. It is also reported that the other real space methods namely successive random addition (SRA) and random midpoint displacement (RMD) are bound to spectral artefacts. The methodology used to generate the rough surface is given here. First the minimum and maximum wave numbers corresponding to the smallest and largest length scale roughness (spectral width) are specified. Subsequently, using the Box-Muller transform random variables U_1 and U_2 are generated in the interval [0,1]. The real and imaginary parts of the Fourier space Gaussian is calculated as

$$\begin{aligned}
\mathcal{R}\{\tilde{\Delta}_{\mathrm{G}}\}(\mathbf{q}) &= w_{\mathcal{R}\{\tilde{\Delta}_{\mathrm{G}}\}}\sqrt{-2\ln\left(U_1\right)}\cos(2\pi U_2);\\
\mathcal{I}\{\tilde{\Delta}_{\mathrm{G}}\}(\mathbf{q}) &= w_{\mathcal{I}\{\tilde{\Delta}_{\mathrm{G}}\}}\sqrt{-2\ln\left(U_1\right)}\sin(2\pi U_2),
\end{aligned} \tag{5.3}$$

where real $w^2_{\mathcal{R}\{\tilde{\Delta}_{\mathrm{G}}\}}$ and imaginary parts $w^2_{\mathcal{I}\{\tilde{\Delta}_{\mathrm{G}}\}}$ of the Fourier space variance are

$$w^2_{\mathcal{R}\{\tilde{\Delta}_{\mathrm{G}}\}} = \frac{(1+\delta_{\mathbf{q},0})}{2nx},\ w^2_{\mathcal{I}\{\tilde{\Delta}_{\mathrm{G}}\}} = \frac{(1-\delta_{\mathbf{q},0})}{2nx}. \tag{5.4}$$

Where $\delta_{\mathbf{q},0}$ is the Kronecker delta and nx is the discretization. The surface topography in Fourier space is thereby calculated as

$$\tilde{h}(\mathbf{q}) = \frac{\tilde{\Delta}_{\mathrm{G}}(\mathbf{q})}{(\sqrt{q_x^2 + q_y^2})^{2(1+H)}} \tag{5.5}$$

5.3 Numerical results

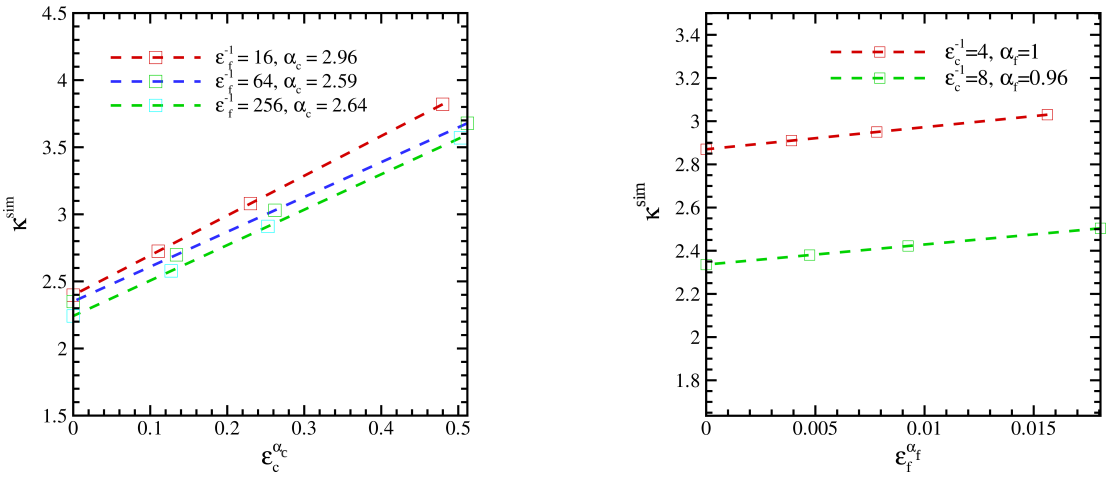

(a) (b)

Figure 5.1: Plot of the proportionality constant κ as a function of continuum discretization ($\alpha_c = 1.468$) a), fractal discretization ($\alpha_f = 1.02$) b)

The κ^{sim} is plotted as a function of the continuum discretization in the Fig.5.1 a) for three cases of spectral width. The continuum limit (ϵ_{c}=0) κ^{sim} value reported in this work (henceforth referred to as κ^{con}) is closer to that estimated in the previous studies of Pradanov *et al.* [3] and Yastrebov *et al.* [23]. Additionally, it can be seen that the κ^{con} marginally scales with the chosen spectral width and this behaviour is in accordance with the work by Yastrebov *et al.* [23]. They showed that for smaller values of the spectral width (corresponding $\lambda_{\mathrm{s}} = 16$), κ^{con} converges to that of the multi asperity contact theories. The dependency of the κ^{con} value on the spectral width could be attributed to the fact that inclusion of more and more surface roughness occurs for higher spectral widths and these additional undulations at the interface leads to lesser values of the contact area fraction. Though the present work only focusses on Hurst exponent H =0, the κ^{con} is expected to decrease with the increase in the H as reported in the previous works. This is due to the fact that roughness lives more strongly on longer wavelengths for higher Hurst exponents and chosen $\epsilon_{\mathrm{c}}^{-1} = 2, 4, 8$ will be able to capture the finest undulations.

Fig.5.1 b) shows the plot of κ^{sim} as a function of fractal discretization, the results showed similar fractal limit (i.e., at ϵ_{f}=0, κ^{sim}=κ^{frac}) value to that estimated in the work of Pradanov *et al.* [3]. It can be seen that for a finer discretization the κ^{frac} is relatively smaller. It is due to the fact that fine discretizations ($\epsilon_{\mathrm{c}}^{-1}$) are able to capture the smallest undulations as for smaller values of H the roughness lives more strongly on shorter wavelengths. Similar to the previous case, we expect the κ^{frac} to scale with the Hurst exponent.

A power law fit is performed to the above curves. The determined the coefficients C_{i} and exponential factors α_{i} corresponding to the discretization are shown in the Tab. 5.2

Reference value	C_{c}	C_{f}	α_{c}	α_{f}
$\epsilon_{\mathrm{f}}^{-1}$ =256, $\epsilon_{\mathrm{c}}^{-1}$ =4	2.64009	10.24	0.991761	1
$\epsilon_{\mathrm{f}}^{-1}$ =256, $\epsilon_{\mathrm{c}}^{-1}$ =8	2.64009	9.31012	0.991761	0.965235

Table 5.2: Coefficients C_i and exponents α_i for κ required to determined κ^{TFC} using Eq. (5.7) for the aspect ratio $a = 1$ and Poisson's ratio $\nu = 0.33$.

The individual corrections to the thermodynamic e_{t}, fractal e_{f} and continuum e_{c} discretizations expressed as

$$\begin{aligned} e_{\mathrm{t}} &= C_{\mathrm{t}}\epsilon_{\mathrm{t}}^{\alpha_{\mathrm{t}}}, \\ e_{\mathrm{f}} &= C_{\mathrm{f}}\epsilon_{\mathrm{f}}^{\alpha_{\mathrm{f}}}, \\ e_{\mathrm{c}} &= C_{\mathrm{c}}\epsilon_{\mathrm{c}}^{\alpha_{\mathrm{c}}} \end{aligned} \tag{5.6}$$

are applied to the κ^{sim} computed for the discretized system,

$$\kappa^{\mathrm{TFC}}\left(\bar{p}/E^*\bar{g}, H\right) = \kappa^{\mathrm{sim}}\left(\bar{p}/E^*\bar{g}, H, \epsilon_{\mathrm{t}}, \epsilon_{\mathrm{f}}, \epsilon_{\mathrm{c}}\right) - C_{\mathrm{t}}\epsilon_{\mathrm{t}}^{\alpha_{\mathrm{t}}} - C_{\mathrm{f}}\epsilon_{\mathrm{f}}^{\alpha_{\mathrm{f}}} - C_{\mathrm{c}}\epsilon_{\mathrm{c}}^{\alpha_{\mathrm{c}}}. \tag{5.7}$$

The κ^{TFC} formulated for the two different reference values of $\epsilon_{\mathrm{c}}^{-1}$ =4, 8 are respectively 2.2 and 2. It can be clearly seen that the choice of the parameter $\epsilon_{\mathrm{c}}^{-1}$ affects the κ^{TFC}. Thus we expect the above κ^{TFC} value to converge to that of the Persson in the case of much finer continuum discretization. Thus the observed dependency on the choice of discretizations leads us to conclude for a surface topography with H =0, a reference system spectral width ($\epsilon_{\mathrm{f}}^{-1}$) equal to 256 and continuum discretization ($\epsilon_{\mathrm{c}}^{-1}$) equal to 16 could lead to a convergence of ≈ 2 i.e., to the value predicted by that of the Persson's theory.

Chapter 6

Conclusion

In this we work we extended the GFMD technique to 3-D in order to understand the contact mechanical behaviour of realistic self affine rough surfaces. To this end, the project is separated into three phases namely: Derivation, Verification and Application.

6.1 Derivation

We adopted the methodology by Venugopalan *et al.* [10] to derive the analytical solution to the displacement for an 3-D arbitrary boundary value problem. The coupling between the in-plane cosine transform of the normal displacement and in-plane sine transform of the lateral displacements was seen in the case of a sinusoidal displacement prescribed problem (Sec.3.3), this verified the correctness of the analytical solution. From the displacements, we subsequently calculated the areal elastic energy density and thereby the Green's function matrix (Sec.3.4). Under the limiting cases of $q_i z_\mathrm{m} >> 0$ and $q_i z_\mathrm{m} << 0$, the components of the Green's function matrix reduced to that of the 2-D case (Sec. 3.5).

6.2 Verification

The dynamically equilibrated solution for the indentation of a semi-infinite elastic slab by an array of flat rigid punches is compared with the FEM solution. We adopted the methodology by Dokkum *et al.* [11] to derive the damping factor of the slowest mode and equilibrated all the harmonic modes of the system using the critical damping factor of the slowest mode (Sec.4.2). When same discretization was given for the surface layer in both the numerical methods, the error between GFMD and FEM results was found to be ≤ 0.2 % (Sec.4.3).

6.3 Application

Finally, we use the 3D-GFMD for the determination of the continuum mechanical proportionality constant κ^{TFC} of a compressible finite slab. The following observations are made (Sec.5.3): The continuum limit value κ^{con} was found to be closer to that predicted in the work of Prodanov *et al.* [3]. Additionally we saw a marginal scaling in the κ^{con} value with fractal discretization.

The fractal limit value κ^{frac} for a continuum discretization of 4 was found to be around 2.87, this was closer to the value predicted in the work of Prodanov *et al.* [3]. Importantly, we saw that the choice of continuum discretization strongly influences the κ^{frac} value and thereby the κ^{TFC} value. For two different continuum discretizations of 4 and 8 we predicted the κ^{TFC} to be around 2 and 2.2 respectively. We conclude that for a reference system having spectral width (ϵ_f^{-1}) equal to 256 and continuum discretization (ϵ_c^{-1}) equal to 16 could lead to a convergence of ≈ 1.65 i.e., to the value predicted by that of the Persson's theory.

Chapter 7

Recommendations

Initially an attempt was made to extend GFMD to be able to model finite-strain problems. To this end, it was therefore decided to break down the finite-strain problem into infinitesimal small-strain problems. Thus as a first step it was decided to relax the small-slope approximations, however the effect of Fourier transformation converted the generic partial differential equation (Sec.3.3) into a flat boundary ordinary differential equation, which thereby currently limited the applicability of this technique to finite-strain problems. Therefore, one of the recommendation will be to relax the small-slope assumption in GFMD.

With the extension of the GFMD successfully made to solve 3-D boundary value problems with single undulations (i.e bottom fixed), the immediate step will be to extend it to solve generic boundary value problems where the bottom is also not fixed. Once extended GFMD can be merged with DDP to obtain a 3-D GFDD (Green's function discrete dislocation dynamics) model to be able to study contact mechanics of rough metallic bodies [13].

Bibliography

[1] J. Greenwood and J. Williamson, "Contact of nominally flat surfaces," *Proceedings of the Royal Society of London A: Mathematical, Physical and Engineering Sciences*, vol. 295, no. 1442, pp. 300–319, 1966.

[2] B. Persson, O. Albohr, U. Tartaglino, A. Volokitin, and E. Tosatti, "On the nature of surface roughness with application to contact mechanics, sealing, rubber friction and adhesion," *Journal of Physics: Condensed Matter*, vol. 17, no. 1, p. R1, 2004.

[3] N. Prodanov, W. B. Dapp, and M. H. Müser, "On the contact area and mean gap of rough, elastic contacts: Dimensional analysis, numerical corrections, and reference data," *Tribology Letters*, vol. 53, no. 2, pp. 433–448, 2014.

[4] F. P. Bowden and D. Tabor, *The friction and lubrication of solids*, vol. 1. Oxford university press, 2001.

[5] H. Hertz, "Uber die Beruhrung fester elastischer Korper," *Journal fur die reine und angewandte Mathematik*, vol. 92, pp. 156–171, 1882.

[6] J. Greenwood and J. Tripp, "The contact of two nominally flat rough surfaces," *Proceedings of the institution of mechanical engineers*, vol. 185, no. 1, pp. 625–633, 1970.

[7] A. Bush, R. Gibson, and T. Thomas, "The elastic contact of a rough surface," *Wear*, vol. 35, no. 1, pp. 87–111, 1975.

[8] S. Hyun and M. O. Robbins, "Elastic contact between rough surfaces: Effect of roughness at large and small wavelengths," *Tribology International*, vol. 40, no. 10, pp. 1413–1422, 2007.

[9] V. A. Yastrebov, J. Durand, H. Proudhon, and G. Cailletaud, "Rough surface contact analysis by means of the finite element method and of a new reduced model," *Comptes Rendus Mécanique*, vol. 339, no. 7-8, pp. 473–490, 2011.

[10] S. P. Venugopalan, L. Nicola, and M. H. Müser, "Green's function molecular dynamics: Including finite heights, shear, and body fields," *Modelling and Simulation in Materials Science and Engineering*, vol. 25, no. 3, p. 034001, 2017.

[11] J. V. Dokkum, "Contact between rough surfaces: A green's function molecular dynamics approach," *Unpublished master thesis, TU Delft*, 2017.

[12] M. Frigo and S. G. Johnson, "The design and implementation of FFTW3," *Proceedings of the IEEE*, vol. 93, no. 2, pp. 216–231, 2005.

[13] S. Venugopalan, M. Müser, and L. Nicola, "Green's function molecular dynamics meets discrete dislocation plasticity," Modell. Simul. Mater. Sci. Eng., submitted(2017).

[14] M. Ciavarella, J. Greenwood, and M. Paggi, "Inclusion of interaction in the Greenwood and Williamson contact theory," *Wear*, vol. 265, no. 5, pp. 729–734, 2008.

[15] G. Carbone, "A slightly corrected Greenwood and Williamson model predicts asymptotic linearity between contact area and load," *Journal of the Mechanics and Physics of Solids*, vol. 57, no. 7, pp. 1093–1102, 2009.

[16] C. Campañá and M. H. Müser, "Contact mechanics of real vs. randomly rough surfaces: A Green's function molecular dynamics study," *EPL (Europhysics Letters)*, vol. 77, no. 3, p. 38005, 2007.

[17] L. Verlet, "Computer experiment of classical fluids. i. thermodynamical properties of Lennard-Jones molecules," *Physical Review 159,* ***98***, 1967.

[18] X.-P. Xu and A. Needleman, "Void nucleation by inclusion debonding in a crystal matrix," *Modelling and Simulation in Materials Science and Engineering*, vol. 1, no. 2, pp. 469–493, 2017.

[19] "Fracture mechanical characterisation of mixed-mode toughness of thermoplast/glass interfaces," *Computational Materials Science*, vol. 19, no. 1, pp. 223 – 228, 2000.

[20] P. S. M.J. Van Den Bosch and M. Geers, "An improved description of the exponential xu and needleman cohesive zone law for mixed- mode decohesion," *Engineering Fracture Mechanics*, vol. 1, no. 73, p. 12201234, 2006.

[21] J. P. McGarry, É. Ó. Máirtín, G. Parry, and G. E. Beltz, "Potential-based and non-potential-based cohesive zone formulations under mixed-mode separation and over-closure. Part I: Theoretical analysis," *Journal of the Mechanics and Physics of Solids*, vol. 63, pp. 336–362, 2014.

[22] B. N. Persson, "Theory of rubber friction and contact mechanics," *The Journal of Chemical Physics*, vol. 115, no. 8, pp. 3840–3861, 2001.

[23] J. M. V.A. Yastrebov, G. Anciaux, "The role of roughness spectral breadth in the elastic contact of rough surfaces," *Journal of Mechanics and Physics of solids*, vol. 107, no. 2, pp. 610–611, 2017.